GNAQ Induces Melanomagenesis in Mitfa-Independent Melanocyte Progenitors in a Zebrafish Model of Uveal Melanoma

Julius I. Yevdash,[1,2] Delaney Robinson,[1] Rachel Moore,[1] Zhijie Li,[1] Katelyn R. Campbell-Hanson,[1] Danielle Gutelius,[3] Stephen P. G. Moore,[3] Dylan Friend,[1] Isaac O'Toole,[1] Brynnon E Harman,[6,7] Collin Montgomery,[1] Robert A. Cornell,[4] Alexander Birbrair,[5] Jesse D. Riordan,[2,8] Adam J. Dupuy,[2,8] Elaine M. Binkley,[2,6,7] Robert F. Mullins,[6,7] Deborah Lang,[3] Ronald J. Weigel,[1,2,8] Colin Kenny[1,2,4,8]

1. Department of Surgery, College of Medicine, University of Iowa, Iowa City, IA 52242, USA.
2. Holden Comprehensive Cancer Center, University of Iowa, Iowa City, IA 52242, USA.
3. Department of Dermatology, Boston University School of Medicine, Boston, MA, 02118, USA.
4. Department of Oral Health Sciences, University of Washington, School of Dentistry, Seattle, WA, 98195
5. Department of Dermatology, University of Wisconsin-Madison, School of Medicine and Public Health.
6. Department of Ophthalmology and Visual Sciences, University of Iowa, Iowa City, IA 52242, Iowa
7. Institute for Vision Research, University of Iowa, Iowa City, IA 52242, Iowa
8. Department of Anatomy & Cell Biology, University of Iowa, Iowa City, IA, 52242, USA.

Running title: GNAQ transforms melanocyte progenitors in zebrafish choroid

* Corresponding author: colin-kenny@uiowa.edu

The authors declare no potential conflicts of interest

Abstract

Melanocytes reside in diverse microenvironments that influence their susceptibility to oncogenic transformation; however, investigation of rare melanoma subsets has been limited by the lack of suitable pre-clinical animal models. Here, we developed a primary, immune-competent zebrafish model to study uveal melanoma (UM) using choroidal melanocyte-targeted injection and electroporation of plasmids encoding human GNAQ^{Q209L} together with CRISPR/Cas9 cassettes for somatic tumor suppressor gene deletion. Single-cell transcriptional profiling of primary melanocytes and melanoma derived from the eye and skin revealed distinct transcriptional programs, with epithelial-to-mesenchymal transition pathways enriched in ocular tumors. In addition, choroidal fibroblasts from tumor-bearing eyes exhibited marked transcriptional changes, including increased fibronectin and collagen expression, consistent with stromal remodeling. Given prior associations between *mitfa* loss and accelerated GNAQ^{Q209L} tumor onset, the model was applied to determine whether melanocyte differentiation state contributes to the emergence of GNAQ-driven tumors. The increased susceptibility resulted from expansion of Mitfa-independent melanocyte progenitor populations in germline *mitfa* mutant zebrafish, rather than somatic *mitfa* loss in differentiated melanocytes, as conditional, melanocyte-specific *mitfa* deletion in adult zebrafish did not accelerate tumor growth. Furthermore, *pax3a*-positive melanocyte progenitor cells in *mitfa*-deficient zebrafish embryos and adult eyes and skin were highly susceptible to transformation induced by GNAQ^{Q209L} but not BRAF^{V600E}. Analogous *PAX3* positive populations were also identified in mouse and human single-cell transcriptomic datasets. Collectively, these findings establish a critical role for Mitfa-independent melanocyte progenitors in UM pathogenesis.

Statement of Significance

Choroid-targeted GNAQ^{Q209L} expression induces anatomically correct uveal melanoma in adult zebrafish, with germline *mitfa* deletion expanding mitfa-independent melanocyte progenitors with enhanced susceptibility that are transcriptionally distinct from the subpopulation transformed by BRAF^{V600E}.

Introduction

Uveal melanoma (UM) is a rare cancer of the melanocytes in the uveal tract. The majority of UM's (~90%) occur in the choroid, the vascular structure supplying the outer retina, with the remainder arising from the ciliary body or the iris.[1] Oncogenic mutations in *GNAQ* or its paralog *GNA11* are observed in up to 90% of UMs but are rare in cutaneous melanoma (CM).[2] Such mutations reduce GTPase activity of the heterotrimeric G protein alpha subunit, resulting in constitutive activation that drives cellular proliferation through downstream signaling pathways, including MAPK, YAP/TAZ, and PI3K.[3,4] The transcriptional mechanisms of UM onset and progression remain understudied, in part, because existing preclinical models inadequately capture the earliest events of ocular melanocyte transformation within the correct microenvironment.

A recent study by Phelps et al.[5] showed that loss of *mitfa,* which is considered the master regulator of the melanocyte lineage, accelerates tumorigenesis in transgenic *Tg(mitfa-GNAQ^{Q209L}); mitfa$^{-/-}$; tp53$^{-/-}$* zebrafish compared to *Tg(mitfa-GNAQ^{Q209L}); tp53$^{-/-}$* controls. These findings indicate that, in the context of tumor-suppressor loss, oncogenic GNAQ can drive tumor formation independently of differentiated melanocytes. This contrasts with *BRAF^{V600E}*-induced melanoma, where Mitfa is required for tumor formation.[6] Such observations imply that melanocyte progenitor cells, which persist in *mitfa*-mutant zebrafish, may serve as the cells of origin for GNAQ-induced transformation. While transgenic models have been incredibly informative for studying spontaneous tumor formation, germline loss of *mitfa* or tumor suppressor genes, together with melanocyte-lineage expression of oncogenes throughout development, may unintentionally perturb melanocyte lineage specification. Consequently, these models may capture tumorigenesis in a lineage already altered during development rather than melanoma initiated by somatic mutations in normal melanocytes. Conditional knockout

approaches as well as lineage restricted expression of oncogenes in the appropriate microenvironment will improve our understanding of UM pathogenesis.

Zebrafish are a well-established model for studying melanocytes and melanoma due to conserved melanocyte differentiation pathways, efficient genetic manipulation, and the availability of transparent lines that facilitate high-resolution live-cell imaging. Zebrafish have three types of pigment cells; dark melanocytes, iridescent iridophores, and yellow xanthophores, that arise from multipotent, neural crest-derived pigment progenitors.[7] To study early events in UM, we developed a novel zebrafish model that utilizes transgene electroporation of adult zebrafish (TEAZ)[8] to express the human *GNAQ*^{Q209L} oncogene and conditionally delete tumor suppressor genes in cells of the melanocyte lineage within the skin and eye. Choroidal targeted injection and electroporation drive primary UM onset from the same anatomical site as human UM. In this study, we demonstrate the existence of a melanocyte progenitor population in zebrafish eyes with increased sensitivity to transformation by GNAQ^{Q209L}. Such progenitor cells are expanded in *mitfa* deficient zebrafish and result in reduced GNAQ^{Q209L}-induced tumor latency compared to wild-type animals.

Materials and Methods

Plasmid constructs and zebrafish generated in this study may be obtained by a request to the lead contact.

Data and code availability

Datasets generated in this article are available from NCBI GEO accession number GEO: GSE307227. This study does not report original code. Any additional information required to reanalyze the data reported in this work paper is available from the lead contact upon request.

Human donor eye procurement and histology

Human donor eyes were obtained from the Iowa Lions Eye Bank with full informed consent from the next of kin for use in research. All procedures adhered to the tenets of the Declaration of Helsinki and institutional guidelines. Globes were processed for histological analysis in the laboratory of Dr. Mullins at the University of Iowa. Tissues were fixed, paraffin embedded, sectioned, and stained with hematoxylin and eosin (H&E) using standard protocols.

Zebrafish husbandry

All zebrafish used in this study were bred and maintained at the University of Iowa Animal Care Facility. The zebrafish are kept consistently at 28°C, 7.4 pH, and controlled salt concentrations and cyclically receive 14 h of light followed by 10 hours of darkness. All zebrafish experiments were performed in compliance with the ethical regulations of the Institutional Animal Care and Use Committee at the University of Iowa and in compliance with NIH guidelines (protocol #3022523). Zebrafish embryos were maintained at 28.5°C and staged by hours or days post-fertilization (hpf or dpf).

Zebrafish mutant lines

Wild-type zebrafish in this study include the *AB* line (RRID:ZFIN_ZDBGENO-960809-7) and the *WIK* line (RRID:ZIRC_ZL84). Transgenic lines include *casper* (*mitfa*$^{w2/w2}$; *mpv17*$^{-/-}$)[9,10] (RRID:ZIRC_ZL1714), *nacre* (*mitfa*$^{w2/w2}$)[11] (RRID:ZIRC_ZL2104), *Tg*(*mitfa*:GFP)[18], and *Tg*(*mitfa*:GFP); *mitfa*$^{w2/w2}$. TEAZ-Eye and TEAZ-Skin was performed on adult zebrafish

(inclusion criteria: greater than 4 months postfertilization and less than 1.5 years old). Similar proportions of male and female zebrafish were used within each experiment.

Induction of melanoma using Strategies A and B.

To model GNAQ-driven melanoma, we generated *mitfa* promoter–driven plasmid systems expressing human oncogenic GNAQ^{Q209L}, CRISPR/Cas9, and guide RNAs (gRNAs) targeting *tp53, ptena, and ptenb*. Two delivery strategies were used. In Strategy A, a single plasmid contained two expression cassettes under the mitfa promoter: one encoding GNAQ^{Q209L} fused to a T2A self-cleaving peptide followed by eGFP, and a second encoding Cas9, together with three U6-driven gRNAs targeting *tp53* and *ptena/b*. Because T2A-mediated cleavage leaves residual C-terminal amino acids that may alter GNAQ oncogenic activity, we also employed an alternative multi-plasmid approach (Strategy B). This system consisted of five separate plasmids: mitfa:*GNAQ^{Q209L}*, mitfa:GFP, mitfa:Cas9, U6:gRNA-*tp53*, U6:gRNA-*ptena*, and U6:gRNA-*ptenb*. Plasmids expressing mitfa:GNAQ^{Q209L} and mitfa:GFP were generously provided by Dr. Jacqueline Lees (MIT), and plasmids encoding Cas9 and gRNAs were provided by Dr. Richard White (University of Oxford). Strategy B was designed to avoid unintended C-terminal modification of GNAQ and to improve electroporation efficiency due to reduced plasmid size. Fish were monitored weekly for tumor formation at the electroporation site. Tumor onset was defined as the first appearance of a visible, expanding pigmented or translucent mass. Tumor latency was calculated as days post-electroporation to first detection. Kaplan–Meier analyses were used to compare tumor onset between experimental groups.

Cloning

The MiniCoopR[6] vector (MiniCoopR 2x*U6*:gRNA, *mitfa*:Cas9 was a gift from Leonard Zon Addgene plasmid # 118844) was modified to replace the *mitfa* coding sequence with *GNAQ*^{Q209L} by removing *mitfa* using StuI and SmaI restriction enzymes (NEB). Gibson assembly was used to insert *GNAQ*^{Q209L}:T2A:GFP DNA as a gBlock hifi (IDT) with sequence on the 3' (GAAGCTAACACATAGTTGAAC) and 5' (CAATGCCAACTAAATTTCATG) as overhangs. Gibson assemblies were transformed using NEB 5-alpha competent *E. coli* cells via heat shock. *GNAQ*^{Q209L}:T2A:GFP insertion was confirmed using Sanger sequencing (Primers: CAAGGAAGCCCGGCGGATCAACGA, CATACTTGTATGGGATCTTGAGTGTGTCCA, GTGGAGTCAGACAATGAGAACCGAATGGAG, CAAGCTGGAGTACAACTACAA).

mitfa sgRNA was designed using IDT's CRISPR-Cas9 guide RNA design tool (sequence: ATGGACAAAGCTGGACCATG). *U6*:sgRNA-*ptena* was linearized by PCR (forward primer: GTTTAAGAGCTATGCTGGAAACAGCAT, reverse primer: GAACAAAGAGCTGGAGGGAG). Linear plasmid was purified from a 2% agarose gel using the Monarch GNA Gel Extraction Kit (#T1020S). ssDNA sequences for sgRNA-*mitfa* were annealed together in NE buffer r2.1. Gibson assembly was used to insert sgRNA-*mitfa* into linearized U6 plasmid. Assembled product was transformed into NEB 5-alpha competent *E. coli* cells via heat shock and selected with 50 ug/mL streptomycin. Insertion of sgRNA-*mitfa* was confirmed using PCR amplification of lysed bacteria from single colonies (forward primer: ATGGACAAAGCTGGACCATG, reverse primer: CTTAGCTGGATAACGCCAC). Positive products were isolated using the QIAGEN Plasmid Maxi Kit. Entire plasmid was sequenced using Plasmidsaurus sequencing service.

Transgene Electroporation of Adult Zebrafish Skin (TEAZ-Skin)

Adult zebrafish were anesthetized in 0.2% Tricaine prior to upright placement on a prewetted Kimwipe. Each injection consisted of 1000 ng total DNA: 100 ng of Tol2 plasmid and an equal

division of the remaining 900 ng for the remaining constructs. Injection stocks contained a small volume (<1uL, 1:50 dilution) of green food coloring to visualize localization of injection. Injection volumes ranged from 1 to 1.5 uL depending on the injection mix, keeping 1000 ng total constant. Needles were pulled from 10 cm long filamented borosilicate glass capillaries at a pressure of 500, heat of 650, pull strength of 100, velocity of 200, and time delay of 40 in a Model P-97 Flaming/Brown micropipette puller from Sutter Instrument Co. Following injection, zebrafish were immediately electroporated (<1 min) by placing the cathode probe of ultrasound gel-coated Platnium Tweezertrode, 3MM, on the side of the injection site and the anode probe on the other side of the fish body. Electroporation was achieved with 5 60-ms pulses of 40 volts with a 1s pulse interval from a ECM 830 Electro Square Porator from BTX Harvard Apparatus. Following electroporation, zebrafish are placed into a recovery tank with fresh, gently stirred system water and are monitored until normal swimming resumes. Electroporated zebrafish are imaged weekly. *mitfa*:*GNAQ*^{Q209L}; *mitfa*:GFP plasmid constructs were kindly provided by Dr. Jacqueline A. Lees (Massachusetts Institute of Technology, Cambridge, USA). *mitfa*:Cas9, *mitfa:*tdTomato, PCS2FA Tol2, *U6*:gRNA-*tp53, U6*:gRNA-*ptena,* and *U6*:gRNA-*ptenb* plasmids were kindly provided by Dr. Richard White (Sloan Kettering Institute, New York, USA).

Transgene Electroporation of Adult Zebrafish Eye (TEAZ-Eye)

Pre-injection preparation for eye injections is the same as for skin injections including: 0.2% Tricaine anesthesia, needle size, and injection concentrations. To inject the eye, a blunt spherical head of a pin was gently pressed against the bottom half of the zebrafish eyeball to reveal the dorsal posterior regions of the eye. The needle was gently pressed into this location, where the cornea is softer, just through the sclera, keeping the needle as superficial as possible as to not damage the back of the eye. Injection volumes were around 0.25 uL and were terminated with a slight visual swelling of the eye. Following injection zebrafish were

immediately electroporated (<1 min) by the cathode probe of ultrasound gel-coated Platnium Tweezertrode, 1MM, on the superior side of the eye nearest the injection and the anode probe on the inferior side of the eye. Electroporation was achieved with 3 50-ms pulses of 75 volts with a 1s pulse interval from a ECM 830 Electro Square Porator from BTX Harvard Apparatus. Recovery and imaging procedures for these fish did not differ from the skin injections.

Imaging and image processing

Injected zebrafish were imaged using an upright Leica M205 FCA microscope with brightfield and GFP filters. Zebrafish were briefly anesthetized with 0.2% Tricaine and positioned on a Kimwipe mound for upright orientation. Images were taken and processed through the LAS X software. All histology slides were imaged using brightfield, DAPI, and GFP filters on an EVOS M5000 microscope from Invitrogen for individual images or on a Leica DMi8 microscope and stitched together by LAS X Thunder Imaging software for full tissue images.

H&E and IF – zebrafish tissue

Whole zebrafish or zebrafish eyes were fixed in 4% paraformaldehyde for 48 hours at 4°C and paraffin embedded in the University of Iowa Pathology Core. Fish were sectioned at 7 µM thickness and placed on Superfrost Plus Microscope slides from Fisher Scientific, baked at 60°C, stained with hematoxylin and eosin, and mounted with Cytoseal 60 from Epredia. For immunofluorescence, sections were deparaffinized and hydrated followed by heat-induced antigen retrieval with 10 mM Na-citrate buffer and blocking with 3% milk in 0.1% Tween 20. slides were stained with primary antibodies against GFP (NB600-308 Rabbit anti-GFP polyclonal from Novus Biologicals, RRID:AB_10003058, at 1:250) overnight at 4°C and then fluorescent secondary antibodies against rabbit IgG (Alexa Fluor 488 goat anti-rabbit IgG,

RRID:AB_2576217, at 1:500 from a 2 mg/mL stock) for 1 hr at room temperature. RPE autofluorescence was minimized using the Vector TrueVIEW Autofluorescence Quenching Kit. Sections were counterstained with DAPI, mounted using VECTASHIELD Vibrance Antifade Mounting Medium, and imaged the same day.

IF - mouse eye tissue

C57BL/6 mice (RRID:MGI:2159769) eyes were collected, formalin-fixed, paraffin-embedded, and sectioned into 7 µm-thick sections. Sections were deparaffinized and hydrated followed by heat-induced antigen retrieval with citrate buffer (Vector Laboratories, Inc.), permeabilized with 1% horse serum in 0.2% Triton-X, blocked with 5% Horse serum in 0.2% Triton-X, and incubated with PAX3 primary antibody (Invitrogen 38-1801 Rabbit anti-PAX3 polyclonal, RRID:AB_2533359, at 1:200) overnight at 4°C. Samples were incubated with DyLightTM 488-labeled secondary antibody (Vector Laboratories, DI-1088-1.5, horse anti-rabbit, RRID:AB_2336403, at 1:2000) for 1 hr at room temperature, treated with autofluorescence quenching kit (Vector Laboratories, Inc. SP-8400-15), and cover slips fitted using Vectashield Antifade Mounting Medium with DAPI (Vector Laboratories, Inc. H-1000-10).

Kaplan-Meier analysis

Zebrafish were followed for up to 70 weeks and tumor-free survival was analyzed with the Kaplan-Meier method. Tumors were defined as the first presence of a GFP-positive nodular mass at the injection site. Zebrafish were excluded from curves if they perished or were euthanized without any visible signs of tumors during the study. Differences between injection groups were analyzed using log-rank statistics.

Single cell suspension and single-cell RNA Seq analysis

Zebrafish were euthanized with 0.4% Tricaine for 10 mins followed by immersion in ice water until no opercular movement was observed for at least 30 min as detailed in our IACUC protocol. Tumors were harvested and minced into small pieces. Minced tumors were digested for 1 hour at 37°C with collagenase and hyaluronidase in HBSS with 2% FBS (HF). Suspensions were washed with 1:4 HF:NH_4Cl and then further digested for 5 min with pre-warmed trypsin. Following trypsin inactivation, cell suspensions were washed twice with 10% FBS in HBSS.

Cellular suspensions were loaded on a 10x Genomics Chromium instrument to generate single-cell gel beads in emulsion (GEMs). Approximately 10,000-20,000 cells were loaded per channel depending on the 10x kit used. See figures S5 and S12 for kit information per sample.
Next GEM kit: targeted cell number = 10,000. Single-cell RNA-Seq libraries were prepared using Single Cell 3′ Reagent Kits v2: Chromium Single Cell 3′ Library & Gel Bead Kit v2, PN-120237; Single Cell 3′ Chip Kit v2, PN-120236; and i7 Multiplex Kit, PN-120262 (10x Genomics) and following the Single Cell 3′ Reagent Kits v2 User Guide (Manual Part # CG00052 Rev A).
GEM-X kit: targeted cell number = 20,000. Single-cell RNA-Seq libraries were prepared using Chromium GEM-X Single Cell 3′ Reagent Kits v4: Library Construction Kit C, PN-1000694; Single Cell 3’ GEM Kit v4, PN-1000693; Single Cell 3’ Gel Bead Kit v4, PN-2001128; and Dual Index Kit TT Set A, PN-3000431; and following the Chromium GEM-X Single Cell 3′ Reagent Kits v4 User Guide (Manual Part # CG000731 Rev B). Libraries were sequenced on an Illumina HiSeq 4000 as 2□×□150 paired-end reads. Sequencing results were demultiplexed and converted to FASTQ format using Illumina bcl2fastq software.

A custom reference genome for the Zebrafish was constructed with GRCz11 primary assembly (Ensembl, RRID:SCR_002344) using Cell Ranger (Cell Ranger mkref function). 10X Genomics scRNA-Seq reads were then processed and aligned to this reference with Cell Ranger (Cell Ranger Count function). Further analysis and visualization was performed using Seurat (v4.1.0)[12], cells with fewer than 200 RNA feature counts and greater than 5% mitochondrial contamination were removed with filtering (greater than 15% for wildtype eye samples). RNA counts were normalized, and FindVariableFeatures was run with the following parameters: selection.method = “vst”, nfeatures = 2,000. The cells were originally clustered in a UMAP by RunPCA then RunUMAP with dims 1:30. FindNeighbors was run with dims 1:30 followed by FindClusters using a resolution of 0.4. These methods identified up to 20 clusters in individual samples.

For comparative analysis, RNA-seq datasets were integrated together using IntegrateData with dims 1:30. New clusters were generated as before. Clusters were annotated using FindAllMarkers and the top 25 enriched genes in each cluster were compared to the Daniocell dataset[13] and Spectacle[14]. Cluster names were given according to the closest matched cellular population between these two datasets. To determine enriched pathways, *danio rerio* gene names were converted into human Ensembl gene codes with g:Profiler[15] and then data were analyzed with the use of QIAGEN IPA (QIAGEN Inc)[16] and GSEA.[17] Pseudotime was performed using Monocle3 (v0.2.3.0).[18]

Verification of sgRNAs

Zebrafish were euthanized with 0.4% Tricaine for 10 mins followed by immersion in ice water until no opercular movement was observed for at least 10 min as detailed in the IACUC protocol. Tumors were harvested and minced into small pieces. DNA was harvested according

to the DNeasy Blood and Tissue Kit from Qiagen. Regions surrounding cut sites were PCR-amplified and the purity of the PCR amplicon was confirmed with agarose gel electrophoresis. Samples were cleaned up with the QIAquick PCR Purification Kit from Qiagen and sent for Sanger sequencing at the Iowa Institute of Human Genetics. Gene editing was confirmed with DECODR INDEL analysis by comparing to wildtype sequence[19]. PCR primer sequences follow:

mitfa PCR F: CCGGTATGTATTCACATTGTCTTG

mitfa PCR R: TCTTGCTTAGGATGCCTATGTATT

ptena PCR F: CATCCCACCAAGTGAGGTTAAAC

ptena PCR R: CACATACACAGTCAAGGGTGAG

ptenb PCR F: CAGTTCTGTTGCACCCAATAAG

ptenb PCR R: CTGGTGGTGTTGAGGCTATAAAG

tp53 PCR F: AAGTATTCAGCCCCCAGGTG

tp53 PCR R: CGCTTTTGACTCACAGTGCAAG

Results

Generation of GNAQ-driven melanoma in adult zebrafish

To model GNAQ-driven melanoma in adult zebrafish, we generated *mitfa* promoter-driven plasmid systems expressing oncogenic GNAQ^{Q209L}, Cas9, and gRNAs targeting *tp53* and *ptena/b* (**Figure 1A**). We tested two delivery strategies: a single-plasmid GNAQ-T2A-GFP construct incorporating all expression cassettes (**Strategy A**), and a multi-plasmid approach designed to avoid C-terminal modification of GNAQ by the T2A cleavage site while improving electroporation efficiency through the use of smaller individual plasmids (**Strategy B; see Methods**).TEAZ applied to adult zebrafish skin (TEAZ-Skin) induced melanoma in wild-type

animals using either strategy, with Strategy B significantly reducing tumor latency (**Figure 1C–D, Figure S1A**). Melanomas developed exclusively from clonal expansion of cells harboring edits introduced by all gRNAs. Neither oncogenic GNAQ expression nor individual tumor suppressor loss alone was sufficient to drive tumorigenesis, demonstrating that combined oncogenic signaling and inactivation of all gRNA-targeted tumor suppressors were required for transformation (**Figure S1A**). Consistent with prior reports, loss of *mitfa* markedly accelerated tumor onset following TEAZ-Skin, with tumors arising within ~30 days in *nacre* (*mitfa*$^{w2/w2}$) and *casper* (*mitfa*$^{w2/w2}$, *mpv17*$^{a9/a9}$) zebrafish (**Figure 1C–D, Figure S1B–D**). In these backgrounds (**see Methods**), oncogenic GNAQ alone was sufficient to drive melanoma, consistent with increased susceptibility of Mitfa-independent cells. Tumor identity was distinguished from xanthomas by gross morphology and pigmentation (**Figure S1E**), and CRISPR-mediated editing of target genes was confirmed by Sanger sequencing (**Figure S2**). Together, these data demonstrate that TEAZ-Skin efficiently induces GNAQ-driven melanoma in adult zebrafish, with Strategy B providing faster tumor onset than Strategy A and *mitfa* loss substantially accelerating disease compared to TEAZ-Skin in wild-type zebrafish (**Figure 1C–D**).

The *mitfa* promoter is active in choroidal melanocytes

We next sought to adapt the TEAZ approach to induce melanocyte transformation in the zebrafish eye (TEAZ-Eye)**.** The zebrafish and human eye share highly conserved overall organization and cellular composition (reviewed in [20]), including distinct retinal layers, retinal pigmented epithelium, and a melanocyte-containing choroidal layer. Most major human ocular compartments have clear zebrafish counterparts, although the zebrafish lacks a fovea and has a proportionally thinner choroid (**Figure 1E**). We first assessed specificity of the *mitfa* promoter in driving transgene expression in choroidal melanocytes by performing immunofluorescent imaging with an anti-GFP antibody in eyes harvested from transgenic *Tg(mitfa:GFP)* zebrafish.

Choroidal melanocytes exhibited strong GFP positivity compared to the secondary antibody-only control (**Figure 1F**). Quenching autofluorescence signal from RPE improved the signal-to-noise ratio (**Figure S3A-B**). We next applied TEAZ-Eye by injecting and electroporating plasmids containing *mitfa* promoter-driven *GFP* expression (*mitfa:GFP*) into the choroid. Eyes were harvested two weeks post-electroporation to assess GFP expression by immunofluorescence. Cells at the injection site exhibited strong GFP signal compared to the secondary antibody-only control (**Figure S3C**), demonstrating that the *mitfa* promoter is sufficient to drive transgene expression in choroidal melanocytes using TEAZ-Eye.

TEAZ-Eye induces UM in the choroid of wild-type and *casper* zebrafish

A major limitation in the study of UM onset and progression is the lack of anatomically accurate *in vivo* models. To address this gap, we used the TEAZ-Eye technique to introduce oncogenic GNAQ and tumor suppressor gRNAs into the choroidal space of wild-type zebrafish (**Figure 1G-H**). Remarkably, TEAZ-Eye in wild-type zebrafish promoted transformation of cells within the choroid. Live *in vivo* imaging of TEAZ-Eye enabled identification of individual GFP+ cells at the injection site, serving as a proxy for $GNAQ^{Q209L}$ expression (**Figure 1H-H'**). We next applied TEAZ-Eye to *mitfa*-deficient *casper* zebrafish (**Figure 1I-I'**). As with TEAZ-Skin, tumor latency of TEAZ-Eye injected *casper* zebrafish (n=13) was significantly reduced compared to wild-type (n=5) (**Figure 1J**). H&E analysis confirmed that TEAZ-Eye induced UM within the choroid, progressing into surrounding ocular structures (**Figure 1K**). Notably, 100% (n=10) of tumors formed between the sclera and RPE, highlighting the model's ability to induce anatomically accurate UM. Finally, anti-GFP immunofluorescent analysis confirmed expression of plasmid constructs following TEAZ-Eye (**Figure 1K'**).

UM transformation involves activation of neural crest transcriptional programs

During embryonic development, choroidal melanocytes are derived from the cranial neural crest (CNC).[21] Since our model can detect the earliest events in UM transformation, we asked whether reactivation of CNC programs is one of the initial steps in UM development. To address this point, tumors were derived in wild-type zebrafish using TEAZ-Eye with Strategy B plasmids. At 50-90 dpe, when gross nodular tumors were identified, surgical enucleation was performed, and dissociated cells from the entire eye were subjected to single-cell RNA sequencing (scRNA-Seq). We compared pooled wild-type tumors (2 sequencing replicates) with tumor-free paired eyes or sibling-matched control eyes (2 and 4 pooled eyes, respectively, 2 sequencing replicates) (**Figure 2A, Figure S4**). Given that whole eyes were used as control samples and melanocytes are most abundant in the choroid, melanocytes identified under control conditions are hereafter referred to as choroidal melanocytes. Tumor cells were identified by expression of *GFP* and oncogenic *GNAQ* (**Figure 2B**) whereas primary choroidal melanocytes were marked by expression of *mlana* (**Figure S5**). Annotation of additional cell types within the TME was accomplished by comparing to previously published human choroid and retina scRNA-Seq datasets,[14,22] the Zebrafish Information Network (ZFIN),[23] and from the zebrafish embryo single cell atlas "Daniocell"[13] (**Figure 2A**). Interestingly, tumor cells aligned most closely with choroidal melanocytes, ruling out the retinal pigmented epithelium (RPE) as an origin of our TEAZ-Eye induced tumors (**Figure 2C**). Additionally, profiling *GFP/GNAQ*^{Q209L}+ UM cells revealed that tumors exhibited strong expression of neural crest markers (*tfap2a, tfap2c, pax7b, sox10, foxd3*) and melanocytic markers (*mitfa, tfap2e, kita, mlana, pmela, slc22a7a, mlpha, mtbl*) (**Figure 2D**). Unexpectedly, CNC marker genes *twist1* or *dlx1*[24,25] were not enriched in UM tumors compared to TME. Pathway analysis showed that genes enriched in TEAZ-Eye-derived tumors were strongly associated with MITF-M-dependent gene expression, RAF/MAP kinase, mTOR, PI3K/AKT signaling, NF-kB, RHO GTPase, and NOTCH activity, as well as fatty acid oxidation pathways (**Figure S6A-B**).

Re-clustering of choroidal cells from control and tumor conditions revealed a marked expansion of tumor cells relative to melanocytes, accompanied by increases in immune cells and fibroblasts (**Figure 2E-F**). Immune cell populations within the TME included B-cells (*igic1s1, pax5, cd79a, zgc:153659*), T-cells (*traf1, si:ch211-67e16.3, cd27, zap70, cd8a, sla2*), a population of cytokine producing cells, likely representing T-cells (*il4, il13, il11, ca2, il34, il6*) as well as macrophages (*marco, ccl34a.4, mrc1b, c1qa/b/c, grn1*) and neutrophils (*cpa5, lect2l, mmp9, npsn, scpp8*). Additional cell types within the choroidal TME included fibroblasts (*fn1a*, *col1a1a, col1a1b, col1a2, col5a1, dcn, serpinf1*), pericytes (*pdgfrb, notch3, foxf2b, cd248a*), Schwann cells (*dlx5a, apoda.1, mpz, plp1b, cd59, s100b, mbap*) and vasculature endothelial cells (*vwf, flt4, epas1b, ecscr, fabp11a*) (**Figure 2D-F**, **Table S1**).

We next compared choroidal melanocytes and UM tumors, revealing a significant overlap in gene expression (n=644; hypergeometric $p<0.0001$) alongside a large set of tumor-enriched genes (n=1177) (**Figure 2G**). Shared genes included melanocytic regulators (*ednrb, sox10, foxd3, mitfa, mlpha, kita, mlana, pax7b*), supporting a melanocytic origin, with many transcripts further upregulated in UM tumors compared to choroidal melanocytes (**Figure 2H**). HOMER promoter motif enrichment analysis of genes enriched in UM tumors revealed binding motifs for the MiT/TFE family of transcription factors, as well as PAX3/7 and HOXB13, suggesting that these regulators may contribute to UM-specific transcriptional programs (**Figure 2G'**).
To assess the relevance of our model to human disease, we examined whether genes enriched in zebrafish UM tumors were associated with clinical outcomes in patients. Differential expression analysis identified a gene signature, including *LGALS2, FABP3/5, GCH, MET*, and *KIT*, whose high expression was associated with reduced overall and disease-free survival and with TCGA molecular subtypes 3 and 4,[26] corresponding to aggressive UM (**Figure 2G, 2I-K, Figure S7-8, Table S2**).

Cancer associated fibroblasts within the uveal melanoma TME upregulate components of the extracellular matrix (ECM)

Recent studies have significantly advanced our understanding of the TME as an active driver of melanoma progression.[27,28] While it is well established that components of the TME, particularly cancer-associated fibroblasts (CAFs), play a key role in malignancy,[29-31] *in vivo* models to study such interactions in UM remain limited. Our model allows for direct comparison of the microenvironment in TEAZ-Eye and control injected eyes within the same animals (i.e., left and right eye). We compared the transcriptome of CAFs and normal fibroblasts in wild-type zebrafish. Upon re-clustering and differential gene expression analysis, we found that several ECM proteins were upregulated in CAFs, indicating ECM remodeling in the presence of UM. Enriched genes broadly fell into four categories: ECM, ECM regulators, TNFs, and collagens. Notably, fibronectin (*fn1a*) was among the most significantly upregulated genes in CAFs compared to normal fibroblasts ($q<0.0001$). Several collagens were also found to have higher expression in CAFs, including Collagen I (*col1a1b, col1a2),* Collagen V (*col5a1, col5a2a, col5a3a)* and Collagen XII (*col12a1a)* (**Figure 2L, Table S3**)**.** Consistently, cell–cell communication analysis using CellChat[32] identified FN1 and collagen signaling from CAFs to tumor cells as significantly enriched pathways and predicted the transmembrane heparan sulfate proteoglycan SDC4 as a mediator of these interactions in UM cells (**Figure S9**).

To control for injection-related fibrosis potentially causing fibroblast activation and upregulation of ECM components, we mock-injected three wild-type eyes with plasmids containing *mitfa*:GFP and *mitfa*:Cas9 cassettes followed by electroporation (mock-TEAZ) and performed scRNA-Seq. Fibroblasts from mock-injected sibling controls (three pooled eyes), non-injected sibling controls (four pooled eyes), and non-injected tumor-matched control eyes (two pooled eyes) were equally distributed on the UMAP, with no alteration in *fn1a* or *lgals2a* expression or other

changes to extracellular matrix (ECM) genes upon mock-TEAZ (**Figure S10**). These findings indicate that TEAZ-Eye tumor induction depends on genetic modification of target cells, not simply physical injection, triggering a CAF response that may be critical to melanoma progression.

Skin and eye primary melanocytes, and their resulting tumors, have unique gene expression profiles

Having established a system to induce genetically identical tumors in the eye and skin of adult zebrafish, we asked whether tumor transcriptional programs differed by anatomical site. Such differences could reflect site-specific tumor–stromal interactions or intrinsic differences between uveal and cutaneous melanocytes. We generated TEAZ-Eye and TEAZ-Skin tumors using Strategy B plasmids and performed scRNA-Seq with matched control eye and skin tissues (**Figure 3A**). We compared tumors to a combined TME and performed a parallel analysis of eye and skin primary melanocytes relative to the combined microenvironment (ME) (**Figure 3B, Table S4**). *GNAQ*^{Q209L} expression levels were comparable between eye and skin wild-type tumors (**Figure S11A**) and DEGs showed substantial overlap between sites, with 41% of 2,192 genes shared, consistent with common transcriptional programs driven by oncogenic GNAQ during transformation (**Figure 3B**). Notably, only 25.8% of DEGs overlapped between eye and skin melanocytes, indicating substantial transcriptional differences in melanocytes originating from distinct anatomical regions (**Figure 3B**).

We hypothesized that DEGs shared by only the two tumor sites and not the primary melanocytes would represent essential mechanisms for UM growth and survival. Consistent with this hypothesis, pathway analysis revealed enrichment of pathways involved in cancer proliferation and metabolism (**Figure S12A**). Additional enriched pathways included WNT signaling, PTEN regulation, and RAF/MAPK signaling, which have been previously implicated in

UM pathogenesis.[33-41] In contrast, IPA analysis of gene sets shared between eye and skin melanocytes represented homeostatic pathways including enrichment of MITF-M–dependent programs, as well as pathways related to nucleotide biosynthesis and mTORC1-regulated amino acid metabolism (**Figure S12B**).

We next re-clustered normal melanocytes from eye and skin for direct comparison, revealing distinct UMAP clusters (**Figure 3C**). We identified 186 DEGs enriched in eye melanocytes and 229 DEGs enriched in skin melanocytes (log2FC > |0.5|, FDR< 0.01), while 3,387 genes were not differentially expressed (FDR > 0.01, expressed in ≥10% of cells, **Table S5**). GSEA revealed that skin melanocytes were enriched for DNA repair pathways and UV response-associated genes (**Figure 3D**). In contrast, eye melanocytes showed enrichment for pathways involved in UV response downregulation and oxidative phosphorylation. We next re-clustered and directly compared eye and skin tumors, which also separated by tissue of origin on the UMAP (**Figure 3E**). We identified 230 DEGs enriched in eye tumors and 375 DEGs enriched in skin tumors (log2FC > 0.5, FDR < 0.01), while 5,754 genes were not differentially expressed between tumor types. Eye tumors were enriched for epithelial-to-mesenchymal transition (EMT) and selenoamino acid metabolism pathways (**Figure 3F**). In contrast, skin tumors were enriched for PI3K–AKT–mTOR signaling and RHO GTPase–mediated activation and YAP1 activity. Together, these analyses demonstrate that both primary melanocytes and GNAQ^{Q209L}-driven melanomas exhibit site-specific transcriptional programs.

Melanocyte progenitor cells are highly susceptible to oncogenic GNAQ transformation in *mitfa*-deficient zebrafish.

H&E analysis of *nacre* and *casper* zebrafish eyes showed loss of choroidal melanocytes (**Figure 4A**), whereas melanin in the RPE remained less affected, as previously demonstrated.[42]

These observations imply that an *mitfa*-independent melanocyte progenitor cell persists in *nacre* and *casper* eyes and that they are susceptible to oncogenic GNAQ-driven transformation. To identify such cells, we crossed *nacre* (*mitfa*$^{w2/w2}$) with transgenic *Tg(mitfa:GFP)* lines to create *Tg(mitfa:GFP); mitfa*$^{w2/w2}$ zebrafish. We then harvested adult eyes at 5 months and performed anti-GFP immunofluorescence. While GFP+ melanocytes were readily detected in the choroid of *Tg(mitfa:GFP)* zebrafish (**Figure 1F, Figure S3**), staining of *Tg(mitfa:GFP); mitfa*$^{w2/w2}$ eyes revealed rare cells with GFP-positivity (**Figure 4B**). Such GFP+ cells were primarily located in the ciliary body, with isolated cells also found in the choroid, suggesting the persistence of an *mitfa*-independent progenitor population in adult *mitfa*-deficient zebrafish eyes (**Figure 4B**). We next asked whether such cells retain the ability to undergo melanocyte differentiation by using TEAZ-Eye to deliver plasmids containing the *mitfa*-promoter driving expression of *mitfa* (i.e., to overexpress *mitfa* mRNA). Interestingly, re-expression of *mitfa* transcript resulted in expansion of choroidal melanocytes in wild-type animals and rescue of choroidal melanocytes in *mitfa*-deficient (*nacre*) zebrafish as shown by H&E analysis (**Figure S13A-B'**). To assess whether GFP-positive cells are sensitive to oncogenic transformation by GNAQ, we expressed *mitfa*:*GNAQ*^{Q209L} in *Tg(mitfa:GFP); mitfa*$^{w2/w2}$ zebrafish using TEAZ-Eye. In all injected fish (n=3), UM tumors were GFP-positive, suggesting they originated from GFP+ progenitor cells within the eye of *Tg(mitfa:GFP); mitfa*$^{w2/w2}$ zebrafish (**Figure S13C**).

Melanocyte progenitor cells express neural crest marker genes in *mitfa*-deficient zebrafish.

We performed scRNA-Seq and pseudotime analysis on 3 pooled UM tumors from the eyes of *casper* zebrafish and compared them to the pooled tissue from 3 normal *casper* eyes (**Figure 4C, Figure S14**). Within the *casper* eyes, we identified a population of cells expressing the *mitfa*$^{w2/w2}$ allele that clustered closely with UM tumors under TEAZ-Eye conditions, termed

progenitors (**Figure S15A-B and Tables S6-8**). We re-clustered the progenitor and tumor cells (**Figure 4D**), revealing seven distinct clusters consisting of neural crest-like (NC-like), melanoblast-like, proliferating, progenitor, angiogenic, stress-like, as well as an unidentified cluster marked by *tmsb1, krt91* and *vim* (**Figure 4D, Table S9**). Unsupervised pseudotime analysis supports a lineage trajectory from the progenitor cells to heterogeneous UM tumor cells (**Figure S15C**). Notably, the progenitor cell population in normal *casper* eyes expressed neural crest and melanocyte stem cell marker genes, including *tfap2a, foxd3, sox10*, *pax3a, vim,* and *yap1* (**Figure 4E-F**). UM tumor cells retained expression of these genes but activated additional genes associated with pigment progenitor cell function, including *tfec* and *kita* (**Figure 4F**). Notably, *mitfa* expression in tumors and progenitor cells in *casper* zebrafish reflects the expression of the mutant *mitfa*$^{w2/w2}$ allele, which functions as a lineage tracer to mark cells that would normally express *mitfa* under wild-type conditions (**Figure S15B**). Interestingly, despite the lack of Mitfa activity in *casper* zebrafish, GNAQ^{Q209L}-positive UM tumors included a melanoblast-like cluster that exhibited expression of pigmentation genes, including *pmela, mlpha*, and *mlana,* likely explaining the occasional emergence of melanin within tumors as they progress in *casper* zebrafish.

Conditional deletion of *mitfa* in adult zebrafish fails to recapitulate germline loss-of-function effects on tumor-free survival in GNAQ^{Q209L}-driven melanoma.

We next asked whether the accelerated growth of GNAQ^{Q209L}-driven tumors in *mitfa*-deficient zebrafish was attributable to increased oncogene expression or cell-intrinsic loss of Mitfa in adult melanocytes. scRNA-Seq analysis showed higher GNAQ^{Q209L} expression in wild-type tumors than in *casper* tumors (**Figure S11B**), thus excluding oncogene overexpression as the basis for the accelerated phenotype. To directly test cell-intrinsic effects of *mitfa* loss in adult melanocytes, we performed conditional somatic deletion of *mitfa* using Strategy B plasmids with

either non-targeting gRNAs or gRNAs targeting exon 5 of *mitfa*. TEAZ-Skin was conducted in three groups: (1) *casper* zebrafish with *mitfa*-targeting gRNAs (n=9; which controls for off-target effects of the gRNA and for potential function of the *mitfa*$^{w2/w2}$ allele); (2) wild-type zebrafish with non-targeting gRNAs (n=9); and (3) wild-type zebrafish with *mitfa*-targeting gRNAs (n=9). GFP expression was confirmed in all injected animals (**Table S11)**. As expected, by 100 dpe tumors developed in 100% (9 of 9) of *casper* zebrafish. Interestingly, there was no significant difference in tumor latency between wild-type and *mitfa* conditional-KO, with both indicating significantly longer latency than in *casper* animals (**Figure 4G–H**). Thus, somatic loss of *mitfa* in adult melanocytes is insufficient to reproduce the reduced tumor-free survival observed with germline *mitfa* deficiency. Notably, *mitfa*-deficient tumors arising in either background developed distal metastases, a feature not observed in *mitfa* wild-type TEAZ-Skin tumors (**Figure 4H, Figure S16**). Together, these findings argue against Mitfa as a repressor of GNAQ-induced transformation in adult melanocytes and indicate that somatic loss in the adult is insufficient to drive tumor initiation.

mitfa-deficient zebrafish exhibit expanded _pax3a_ and _tfec_ positive melanocyte progenitors during embryogenesis.

We next asked whether melanocyte progenitor cells are expanded in *mitfa* mutant zebrafish relative to wild-type zebrafish. To test this prediction, we performed scRNA-Seq on GFP-positive cells sorted from *Tg(mitfa:GFP);mitfa*$^{w2/w2}$ and *mitfa*$^{+/w2}$ sibling-matched transgenic zebrafish embryos at 28 hours post fertilization (hpf), when melanocytes (zebrafish melanophores) begin to differentiate (**Figure 4I, Figure S14**). We assigned cell-type annotations based on our previously annotated GFP-positive cells from *Tg(mitfa:GFP)* embryos.[43] The 10 clusters included six main cell types: neural crest cells (*sox10, foxd3*), a tripotent precursor of melanoblasts (M), iridoblasts (I), and xanthoblasts (X) (*tfap2a*, *cdkn1ca, slc15a2, ino80e, id3,*

603 *mycn, tfec*), termed MIX cells, a cluster that expressed high levels of melanoblast/xanthoblast
604 markers (*mitfa, erbb3b, impdh1b, gch2, id3*), termed MX cells, a melanoblast cluster (*mitfa, dct,*
605 *pmel, tyr*), as well as two additional clusters corresponding to xanthoblasts and xanthophores
606 (**Table S10**). For this analysis we referred to MIX and MX cells as melanophore progenitors
607 (**Figure 4I**). As expected, melanophore cells were reduced in *Tg(mitfa:GFP): mitfa*$^{w2/w2}$ zebrafish
608 (**Figure 4I'**). However, melanophore progenitors were expanded in *Tg(mitfa:GFP); mitfa*$^{w2/w2}$,
609 while neural crest cells remained unaffected (**Figure 4I-I'**). Melanophore markers were
610 downregulated in GFP-positive cells sorted from *Tg(mitfa:GFP); mitfa*$^{w2/w2}$, whereas melanocyte
611 progenitor markers (*pax3a, sox10, foxd3*), as we identified in adult zebrafish eyes, were
612 upregulated in embryonic progenitors from *Tg(mitfa:GFP); mitfa*$^{w2/w2}$ embryos (**Figure 4J, Table**
613 **S12**). A role for *pax3a* in adult fish eye tissue has not been previously characterized; however,
614 recent studies have identified *PAX3* expression in ocular surface melanocytes,[44] and another
615 study reports an association between *PAX3* and stem cell markers in UM progression.[45]
616
617 **Transcriptional programs enriched in oncogenic BRAF- versus GNAQ-driven melanoma**
618 **overlap with specific melanocyte progenitor populations.**
619
620 Oncogenic BRAF and NRAS are unable to promote transformation in the absence of *mitfa,*[6,46]
621 suggesting that distinct transcriptional programs, potentially reflecting unique cellular origins, are
622 required for UM and CM transformation. To address this hypothesis, we compared previously
623 published scRNA-Seq datasets in transgenic *Tg(mitfa:BRAF*^{V600E}*): tp53*$^{-/-}$: *mitfa*$^{w2/w2}$ zebrafish
624 where TEAZ-Skin was used to rescue *mitfa* and induce melanoma,[46] to our GNAQ^{Q209L}-induced
625 TEAZ-Skin tumors (**Figure 5A)**. We predicted that by analyzing primary tumors, the
626 transcriptional signature of the origin cell will be retained and can be identified by overlapping
627 gene signatures identified in the embryonic melanocyte lineage.[43] Interestingly, while the
628 expression of *mitfa* was significantly higher in GNAQ-positive tumors, the expression of

pigmentation genes; including *tyrp1b, dct, scl45a2, sox10* and *pmela* were significantly higher in BRAF-positive melanoma (**Figure S17**). Genes enriched in GNAQ-UM and BRAF-CM were defined as those with a Log2FC > 1 and Adj p-value < 0.0001 between the two tumor types (**Figure 5B, Table S13**). We next overlapped this differential gene signature with genes expressed by cells within the melanocyte lineage isolated from zebrafish embryos (**Figure 5C**). As expected, BRAF-driven tumors strongly mapped to melanoblast and melanophore clusters (**Figure 5D**), supporting recent findings that BRAF-driven melanoma originates from melanoblasts, a melanocyte progenitor population[46,47]. When comparing GNAQ-enriched genes to the melanocyte lineage, we found that signatures were not confined to a single cluster but were distributed among neural crest cells, melanocyte progenitors, and xanthophore clusters (**Figure 5D; Figure S18**). Such results support the hypothesis that GNAQ- and BRAF-driven melanomas depend on distinct transcriptional programs, reflecting less and more differentiated melanocytic states, respectively.

We next asked whether less differentiated melanocytes, similar to the *mitfa*-deficient progenitors in *casper* eyes, are also present in adult wild-type eyes. Since melanocyte stem cells are known to reside in the zebrafish skin,[48] we included skin tissue as a control and re-clustered melanocytes from wild-type skin and eyes with progenitor cells from *casper* eyes. Interestingly, a subset of wild-type melanocytes from both eye and skin samples clustered closely with *casper* progenitors (**Figure 5E, Figure S19**) and expressed pigment cell progenitor marker genes, including *pax3a,*[49] *tfec,*[42] *sox10,*[50] *sox4a,*[51,52] *foxd3,*[53] and *yap1* (**Figure 5F**). These findings suggest either melanocyte plasticity within the eye or the presence of an eye-resident melanocyte progenitor cell population in adult wild-type zebrafish. In support of this notion, reanalysis of published scRNA-Seq datasets from human[22] and mouse[54] eyes identified *PAX3*-positive melanocyte subpopulations (**Figure S20**) Moreover, we confirmed the presence of PAX3-positive cell populations in adult C57BL/6 mouse eyes by immunohistochemistry (**Figure**

S21). Together, these data support the existence of a *PAX3*-expressing melanocyte precursor population in both fish and mammalian eyes, which may mirror *PAX3* expression in skin melanocyte stem cells.[49,55] Such cells may be more susceptible to GNAQ^{Q209L}-driven transformation and represent candidate cells of origin for UM in this context (**Figure 5G**).

Discussion

Our UM model enables analysis of the earliest events in UM initiation and progression. Compared with transgenic approaches, this system produces anatomically correct tumors with shorter latency. Importantly, genes identified in this model are associated with survival differences in human uveal melanoma, offering an efficient and clinically relevant platform for studying UM pathogenesis.

We found that fatty acid binding proteins, particularly *fabp3*, are enriched in UM tumors. While lipid droplets have been identified as vulnerable targets in CM and regulators of melanoma plasticity,[46,56] lipid signaling in UM has received limited attention.[57-60] Interestingly, high expression of *FABP3* and *FABP5* are associated with worse disease-free survival in UM but not CM patients. Our analysis also identified *LGALS2* and *GCH*, two fatty acid metabolism-related genes whose expression was strongly associated with worse overall survival in UM but showed an inverse relationship in CM. We additionally found increased *kita* expression in GNAQ-driven tumors compared to choroidal melanocytes, which is particularly notable given recent studies linking KIT-positive UM tumors with poor prognosis and chromosome 3 monosomy.[61] In addition, *met* expression was elevated in UM tumors relative to choroidal melanocytes. MET signaling is a key pathway in UM pathogenesis, with established roles in tumor invasion, metastatic progression, and responsiveness to hepatocyte growth factor (HGF), particularly in the context of liver metastasis.[62,63] Notably, MET activation has also been described in other cancer types

through ligand independent fibronectin-integrin α5β1-mediated signaling.[64] Given the marked increase of *fn1a* in choroidal CAFs, it is plausible that fibroblast-driven ECM remodeling enhances MET signaling in UM. Furthermore, expression of these genes was highest in molecular subclasses 3 and 4 of the UM TCGA dataset which represents the subset of patients with the highest rates of BAP1 loss and metastasis.[26] Such observations demonstrate the utility of our model in uncovering key genes with disease-specific roles in UM whose function could be further explored through genetic perturbations in zebrafish.

To explore how anatomical context influences transcriptional states, we compared tumors induced by identical genetic perturbations in the skin and eye. We find that transcriptional profiles of UM tumors arising from melanocytes in the choroid and skin are influenced by more than the intrinsic differences of their cells of origin. For example, eye tumors were enriched for EMT programs compared with skin tumors. In contrast, eye melanocytes did not exhibit these signatures relative to skin melanocytes, suggesting that signals from the ocular microenvironment may promote a more mesenchymal state. Alternatively, these differences may represent a unique cellular origin of UM in the eye and skin. Further investigation is needed to determine whether these differences are driven by the microenvironment or by intrinsic properties of melanocytes or precursors cells from distinct anatomical sites.

An interesting distinction between GNAQ and BRAF oncogenes is their differential dependency on Mitfa activity for tumorigenesis. While $BRAF^{V600E}$ requires Mitfa activity to induce melanoma,[6] $GNAQ^{Q209L}$-driven tumor latency was significantly reduced in *mitfa*-deficient zebrafish compared to wild-type controls. Our results are consistent with prior studies showing that *mitfa*-deficient zebrafish activate distinct signaling pathways, favoring YAP over MAPK signaling, and give rise to tumors with reduced latency compared to wild type tumors.[5] We observed *yap1* expression in melanocyte progenitor cells of *mitfa*-deficient and wild type zebrafish, suggesting that Yap1

activity may be carried over from the progenitor cell during transformation. While germline *mitfa* loss accelerates tumor onset, our data suggest this effect is not solely due to the deletion of Mitfa from differentiated melanocytes. Instead, we propose that germline *mitfa* deficiency expands a population of *pax3a*-positive melanocyte progenitor cells, which are more susceptible to GNAQ-induced transformation. Alternatively, *mitfa* loss may impair the differentiation of melanocyte progenitors, preventing the formation of GNAQ^{Q209L}-positive nevi and promoting direct progression to malignancy. Another explanation for decreased tumor latency in *casper* zebrafish could be that germline loss of *mitfa* has effects on other cell types, such as immune cells, which may influence tumor behavior.

Although Mitfa-independent melanocytic cells are unlikely to be the cellular origin of CM in zebrafish models, studies have shown that MITF-independent BRAF-positive melanoma cells are central to disease recurrence[65]. GNAQ-driven transformation may be facilitated by Mitfa paralogs such as Tfec and Tfeb. The Mitfa paralog Tfec has been shown to activate pigmentation genes in both the retinal pigment epithelium and melanocyte progenitor cells. Tfec can also rescue ectopic melanocytes in *nacre* zebrafish embryos.[42,66] Moreover, we have recently shown that the MITF paralog TFE3 promotes cellular plasticity in MITF-low melanoma cells,[67] suggesting that MITF paralogs are compelling candidate transcription factors to drive UM onset in *casper* zebrafish.

In our zebrafish study, melanocyte progenitors inherently express neural crest-associated programs, which are retained during GNAQ^{Q209L}-driven transformation. Re-analysis of mouse and human single-cell datasets reveals a subpopulation of *PAX3*-positive melanocytes, suggesting that similar progenitor-like states may be conserved in mammals. Together, these findings highlight how lineage plasticity contribute to UM initiation and progression across species. Such observations are supported by an elegant study by Xu, Karreth and colleagues,

who established an immune-competent mouse UM model showing that transcriptional plasticity from melanocytic to neural crest-like states drives tumor progression.[68]

Identifying the transcriptional and signaling mechanisms within *mitfa*-independent melanocyte progenitor cells that facilitate UM onset and progression will have significant clinical implications, particularly for the differential diagnosis of high-risk lesions and the design of targeted therapies.

Limitation of study

The use of *tp53* and *ptena/b* mutations in our UM model does not fully recapitulate the genetics of human UM. Mutations in *TP53* and *PTEN* are rarely observed in UM, where loss-of-function mutations in *BAP1* represent the most frequent tumor suppressor alteration.[39,69,70] However, both *TP53* and *PTEN* signaling pathways have been shown to be altered in UM pathogenesis. *MDM2* overexpression, an upstream negative regulator of p53, and downregulation of *PERP*, a downstream effector of p53, have been demonstrated in many UM patients and are associated with worse outcome.[71-75] Studies have also shown that over half of UM tumors have decreased PTEN immunostaining and its loss is correlated with decreased survival.[39-41] Whether genetic knockout of these tumor suppressors recapitulate the dysregulation of these pathways in human UM remains an open question. Another limitation to our approach when examining the differences between genetically identical skin and eye-derived tumors is the inability to distinguish between microenvironmental effects and differences in cell of origin (melanocytes in the skin versus in the eye). To address this question, a syngeneic or immunodeficient model could be applied to transplant cells from a primary UM tumor into both anatomical sites. Additionally, our use of the *mitfa* promoter to drive oncogene expression presents a challenge in defining the exact cell of origin, as this promoter is active in both melanocyte progenitors and

differentiated melanocytes. As such, it remains unclear whether tumors in *mitfa* wild-type fish (or those with conditional *mitfa* deletion) arise from a progenitor or a mature melanocyte. Lineage tracing studies will be essential to determine whether differentiated melanocytes possess the capacity to initiate primary UM in *mitfa*-competent or conditional *mitfa*-KO zebrafish.

Acknowledgments

This work was supported by the Holden Comprehensive Cancer Center (P30 CA086862). Additional support to C.K. was provided by an institutional research grant from the American Cancer Society administered through the HCCC (IRG-18-164-43), the Melanoma Research Alliance (ID#1426690) and Outrun the Sun in honor of Doug Stickney. J.Y. and D.R. were supported by NIH predoctoral fellowships (T32 GM144636 and T90 DE023520, respectively). Additional NIH support was provided to C.K. (R03 CA297549-01), R.A.C. (R01 AR062457), R.F.M. (P30 EY025580), and D.L. (R03 CA288281-01). Further funding was provided by the Leo Foundation (LF-OC-21-000888) to D.L., the Wisconsin Partnership Program (AAN4246) to A.B., and the U.S. Department of Defense (ME240045) to A.B. The funders had no role in study design; data collection, analysis, or interpretation; manuscript preparation; or the decision to publish.

Figure 1: *GNAQ*^{Q209L}-induced melanoma by TEAZ-Skin and TEAZ-Eye.

(**A**) TEAZ-Skin was used to induce GNAQ-positive melanoma using two strategies. Strategy A involves a single plasmid construct containing expression cassettes driven by the *mitfa* promoter for GNAQ^{Q209L}-T2A-eGFP and Cas9, as well as a U6 promoter driving the expression of three separate gRNAs (targeting *tp53*, *ptena*, and *ptenb*, or a non-targeting control). Strategy B uses a multi-plasmid approach with five plasmids for TEAZ-Skin. Expression cassettes include: (a) *mitfa*:*GNAQ*^{Q209L}-*mitfa*:eGFP, (b) *mitfa*:Cas9, (c) *U6*:gRNA (*tp53*), (d) *U6*:gRNA (*ptena*), and (e) *U6*:gRNA (*ptenb*).

(**B**) Schematic of TEAZ-Skin using wild type (*AB*), *nacre* (*mitfa*$^{w2/w2}$) and *casper* (*mitfa*$^{w2/w2}$*: mpv17*$^{a9/a9}$) zebrafish lines.

(**C**) TEAZ-Skin using Strategy B plasmids in adult wild-type (*AB*) and *casper* zebrafish. Representative brightfield and fluorescent images shown at 4, 8, and 12 weeks post electroporation for WT and at 2, 4, and 6 weeks for *casper*. Scale bar = 0.5 cm.

(**D**) Kaplan-Meier curves were used to estimate tumor-free survival, defined as the time from electroporation until the first visible appearance of GFP+ nodular tumors, in adult zebrafish via TEAZ-Skin. Strategy B wild-type (n=9), *nacre* (n=5), and *casper* (n=24) curves and TEAZ-Skin (*GNAQ*^{Q209L}:GFP) curves (n=3 per condition) compared pairwise with logrank (Mantel-Cox) test. ns = not significant, * p-value<0.05; ** p-value<0.01; ***p-value<0.001; ****p-value<0.0001.

(**E**) Schematic of the zebrafish eye with dashed box indicating the retina and choroid. Comparative H&E of the retina and choroid from a wild-type zebrafish (left) and human donor (right) (20×). Choroidal melanocytes indicated with red arrows. VIT, vitreous; ILM, internal limiting membrane, GCL, ganglion cell layer; IPL, inner plexiform layer, INL, inner nuclear layer; ONL, outer nuclear layer; POS, photoreceptor outer segments; RPE, retinal pigmented epithelium; CH, choroid; SCL, Sclera. Scale bars = 20 μm.

(**F**) Immunofluorescent analysis of transgenic *Tg(mitfa:GFP)* zebrafish using an anti-GFP antibody. Sections were counterstained with DAPI to visualize nuclei. Representative image

showing GFP expression in *mitfa*-positive cells. Secondary-only antibody was used as background control. Scale bar = 50 μm.

(**G**) Schematic of TEAZ-Eye using choroidal targeted injection.

(**H-H'**) Live imaging of adult wild-type zebrafish following TEAZ-Eye with Strategy B plasmids to induce uveal melanoma. Brightfield imaging and the corresponding GFP fluorescence images highlighting tumor progression. Timepoints in day post-electroporation (dpe) as labeled. (H) Scale bar = 250 μm. (H') Scale bar = 0.5 cm.

(**I-I'**) Live imaging of adult *casper* zebrafish over 21 days post-electroporation (dpe) using TEAZ-Eye with Strategy B plasmids to induce uveal melanoma. Brightfield imaging and the corresponding GFP fluorescence images highlighting tumor progression. (I) Scale bar = 250 μm. (I') Scale bar = 0.5 cm.

(**J**) Kaplan-Meier curves comparing tumor-free survival among wild-type (n=5) and *casper* (n=13) zebrafish following TEAZ-Eye induction using Strategy B plasmids. Curves compared pairwise with logrank (Mantel-Cox) test. ** p-value<0.01.

(**K, K'**) H&E analysis of uveal melanoma in *casper* zebrafish induced by TEAZ-Eye. Images were acquired at 20× magnification and stitched from 85 fields using Thunder imaging software. Normal eye tissue and uveal melanoma as labeled. Scale bar = 100 μm.

(**K'**) Representative 40x magnification image showing GFP expression in tumors cells after anti-GFP immunofluorescent analysis of TEAZ-Eye induced uveal melanoma in *casper* zebrafish.

Figure 2: Single cell profiling of uveal melanoma and the TME in adult zebrafish.

(**A**) UMAP representation of single-cell RNA-Seq (scRNA-Seq) from three dissociated wild-type eyes harboring uveal melanoma (UM). UM tumors were generated by TEAZ-Eye (sequencing

replicates, n=2). Control eyes represent pools of two, tumor-free paired wild-type eyes and four sibling-matched wild-type eyes (sequencing replicates, n=2). Annotated cell clusters as labeled.

(**B**) UMAP and feature plot showing *eGFP* and *GNAQ*^{Q209L} expression in control eyes and UM tumor. Red dotted line highlights the melanocyte and UM clusters.

(**C**) Comparison of UM tumor marker genes with the markers of cell types within the control eye microenvironment. Only genes with a log2FC > 1 and FDR < 0.01 were included in the analysis.

(**D**) Dot plot representing enriched genes (log2FC > 1; q-value < 0.01) in choroidal cell populations, UM tumors cells, immune cell populations, fibroblasts, Schwann cells, pericytes, and vascular endothelial cells as shown. Dot size indicates the percentage of cells expressing each gene; color intensity (grey to blue) reflects normalized average expression levels (low to high).

(**E**) UMAP clustering of cells in the choroidal microenvironment. Annotated cell clusters as labelled.

(**F**) Comparison of relative cluster sizes between the two conditions, control and TEAZ-Eye, shown in (E). Schwann cells serve as a control cluster, displaying no change in frequency between conditions. Gray = TEAZ-Eye, Blue = Control.

(**G**) Venn diagram representing the overlap of genes between UM tumors and choroidal melanocytes compared to the cells in their respective microenvironments. Enriched genes for each condition were identified by differential expression analysis comparing melanocytes to the microenvironment (ME) or tumor cells to the tumor microenvironment (TME), using a threshold of log2FC > 1 and FDR < 0.01. Genes of interest have been labelled in their respective subsets, bolded genes represent genes associated with worse overall survival or disease-free survival in human UM TCGA datasets. (G') HOMER promoter motif enrichment analysis of genes enriched in UM tumors vs TME. The top ranked motif for "known" and "*de novo"* motifs are shown with their corresponding p-values.

(**H**) Dot plot showing enriched genes (log2FC > 1; FDR < 0.01) in UM tumor cells, choroidal melanocytes, or the tumor microenvironment (TME). Dot size indicates the percentage of cells expressing each gene; color intensity (grey to blue) reflects normalized average expression levels (low to high).

(**I-K**) Kaplan–Meier disease-free survival and overall survival curves generated using uveal melanoma TCGA data. Patients stratified by relative expression levels of *KIT*, *FABP3*, or *LGALS2*. Gene expression thresholds were defined by median expression within each cohort. Log rank p-values as shown. Dotted lines represent 95% confidence interval.

(**L**) Dot plot showing enriched genes (log2FC > 1; FDR < 0.01) in cancer-associated fibroblasts (CAF), normal fibroblasts (NF), or the tumor microenvironment (TME) without CAF. Dot size indicates the percentage of cells expressing each gene; color intensity (grey to blue) reflects normalized average expression levels (low to high). Genes have been grouped according to their labelled functions.

Figure 3: Comparison of GNAQ-driven tumors and primary melanocytes in the skin and eyes of adult zebrafish.

(**A**) UMAP representation of GNAQ-positive tumors generated using TEAZ-Eye and TEAZ-Skin, along with their respective control tissues using scRNA-Seq. Tumor samples include three dissociated wild-type eyes harboring UM tumors generated via TEAZ-Eye and two dissociated wild-type skin UM tumors generated via TEAZ-Skin (n=2 sequencing replicates each). Control eye samples consist of a pool of two uninjected tumor paired wild-type eyes, three mock-injected sibling-matched wild-type eyes, and four uninjected sibling-matched wild-type eyes (n=3 sequencing replicates). Control skin samples consist of dissociated normal skin from two wild-type zebrafish (n=2 sequencing replicates). Cell clusters are annotated as tumor cells (red

= Eye; Blue = Skin), tumor microenvironment (TME) cells shared by both eye and skin samples (light gray), and TME cells specific to the eye samples (dark gray).

(**B**) Venn diagram showing overlapping genes between TEAZ-Eye, TEAZ-Skin, choroidal melanocytes, and skin melanocytes compared to the cells in their respective microenvironments. Enriched genes for each condition were identified by differential expression analysis comparing melanocytes to the microenvironment (ME) or tumor cells to the tumor microenvironment (TME), using a threshold of log2FC > 0.5 and FDR < 0.01. Bar chart displaying overlaps between enriched gene sets from (B). Percentages represented as the number of overlapping genes over the total unique genes in both gene sets.

(**C**) UMAP representation of primary melanocytes from both eye (salmon) and skin (teal). Volcano plot of differentially expressed genes (DEGs) between eye and skin primary melanocytes (log2FC > |0.5| and FDR < 0.01).

(**D**) GSEA enrichment plots of pathways that were enriched in skin melanocytes and of pathways enriched in eye melanocytes from (C). P-values and FDRs as labelled.

(**E**) UMAP representation of GNAQ^{Q209L}-induced melanoma from both eye (salmon) and skin (teal). Volcano plot of differentially expressed genes (DEGs) between eye and skin tumors (log2FC > |0.5| and FDR < 0.01).

(**F**) GSEA enrichment plots of pathways that were enriched in skin melanoma and of pathways enriched in eye melanoma from (E) P-values and FDRs as labelled.

Figure 4: *mitf*-independent melanocyte progenitor cells are expanded in *mitfa*-deficient zebrafish and are susceptible to *GNAQ*^{Q209L} transformation.

(**A**) H&E analysis representation of the retina and choroid in wild-type (left), *nacre* (middle), and *casper* (right) zebrafish (20x magnification). Note the loss of melanocytes (red arrows) in the choroid of *nacre* and *casper* eyes. “Vit” = vitreous, “GCL” = ganglion cell layer, “INL” = inner

nuclear layer, “ONL” = outer nuclear layer, “POS” = photoreceptor outer segment, “RPE” = retinal pigmented epithelium, “CH” = choroid. Scale bar = 50 μm.

(**B**) Immunofluorescent analysis of transgenic *Tg(mitfa:GFP); mitfa*$^{w2/w2}$ (*nacre*) zebrafish using an anti-GFP antibody. Sections were counterstained with DAPI to visualize nuclei. Representative images showing GFP-positive cells in the ciliary body and choroid are shown by yellow arrow heads. Secondary-only antibody was used as background control. Scale bar = 20 μm.

(**C**) UMAP representation of single-cell RNA sequencing (scRNA-Seq) data from three paired dissociated *casper* eyes and from three *casper* eyes harboring uveal melanoma (UM) tumors induced using Strategy B via TEAZ-Eye (n=1, sequencing replicate). Annotated cell clusters are labeled. Progenitor cells and UM tumor clusters are outlined with dashed red lines. Representative brightfield images of a normal eye and a UM tumor in *casper* zebrafish are shown in the top left corner of the UMAP. Scale bar = 250 μm.

(**D**) Re-clustered UMAP representing progenitor cells from control eyes and uveal melanoma (UM) tumor cells from TEAZ-Eye–injected *casper* zebrafish. Heterogeneous cell populations as labeled.

(**E**) Re-clustered UMAP from (D) showing melanocyte progenitor cells from control eyes in red and UM tumor cells from TEAZ-Eye in blue. Feature plots for *pax3a, foxd3* and *sox10* expression are shown, dashed line marks the progenitor cell population.

(**F**) Dot plot illustrating differentiational expressed genes (log2FC > 0.5; FDR < 0.05) between heterogeneous cell populations in (D). Dot size indicates the percentage of cells expressing each gene; color intensity (blue to red) reflects normalized average expression levels (low to high).

(**G**) Kaplan–Meier curves comparing tumor-free survival in wild-type and *casper* zebrafish following TEAZ-Eye injection using Strategy B plasmids for *mitfa* conditional knockout. Wild-type

zebrafish were injected with either Strategy B plasmids plus non-targeting gRNAs (n=9) or Strategy B plasmids plus *mitfa*-targeting gRNAs (n=9). *Casper* zebrafish were injected with Strategy B plasmids and *mitfa*-targeting gRNAs (n=9).

(**H**) Representative brightfield and GFP-overlay images of tumors that formed in *casper* (9 of 9) and wild-type zebrafish injected with *mitfa*-targeting gRNAs (8 of 9). Metastatic cells are indicated by red arrows. Scale bar = 0.5 cm.

(**I, I'**) UMAP obtained after clustering GFP-positive cells sorted from *Tg(mitfa:GFP)* and *Tg(mitfa:GFP); mitfa*$^{w2/w2}$ (*nacre*) zebrafish embryos at 28 hours post fertilization (hpf). Annotated cell clusters as labelled. (**I'**) Comparison of relative cluster size for the two genotypes; *Tg(mitfa:GFP)* and *Tg(mitfa:GFP); mitfa*$^{w2/w2}$ (*nacre*) in (I). Scale bar = 0.5 mm.

(**J**) Dot plot illustrating DEGs (log2FC > 0.5; FDR < 0.05) in melanophores and progenitor cells in *mitfa*$^{w2/w2}$ and sibling embryos at 28hpf. Dot size indicates the percentage of cells expressing each gene; color intensity (grey to red) reflects normalized average expression levels (low to high).

Figure 5: Oncogenic GNAQ and BRAF transform transcriptionally distinct cells within the melanocyte lineage.

(**A**) UMAP obtained after clustering tumor cells from *Tg(mitfa:BRAF*^{V600E}*): tp53*$^{-/-}$: *mitfa*$^{w2/w2}$ zebrafish where TEAZ-Skin was used to rescue *mitfa* expression and knockout *ptena* and *ptenb* to induce cutaneous melanoma,[46] along with our GNAQ-induced tumors by TEAZ-Skin (Strategy B: *mitfa:Cas9, U6:*gRNA-*tp53, U6:*gRNA-*ptena, U6:*gRNA-*ptenb, mitfa:GNAQ*^{Q209L}-*mitfa:GFP*). BRAF-induced tumors in red and GNAQ-induced tumors in blue.

(**B**) Violin plot showing differentially expressed genes (FDR < 0.05) between BRAF-induced and GNAQ-induced tumors from (A). The plot displays the distribution of gene expression across

individual cells, with the width indicating cell density at specific expression levels and the height representing the range of expression values.

(**C**) Integrated UMAP after clustering GFP-positive cells sorted from *Tg(mitfa:GFP)* and *Tg(mitfa:GFP); mitfa*$^{w2/w2}$ (*nacre*) zebrafish embryos at 28 hours post fertilization (hpf). Annotated cell clusters as labelled.

(**D**) Average enrichment of signature genes from BRAF- and GNAQ-driven tumors projected onto the UMAP in (C) using UCell with 'FeaturePlot' function. Signature genes represent the top 50 enriched genes from each tumor genotype that are also expressed in the embryonic melanocyte lineage.

(**E**) UMAP of primary melanocytes and melanocyte progenitors from 9 control wild-type eyes, 2 control wild-type skin sections, and 3 control *casper* eyes. Cells are labeled according to their genotype (*casper* and wild-type) and tissue origin (eye and skin).

(**F**) Feature plots representing the relative mRNA expression of *pax3a*, *tfec, sox4a, yap1, sox10*, *foxd3* and *ednrba* in melanocytes described in (E). Color intensity (grey to red) reflects normalized average expression levels (low to high). The red dotted line indicates cells that are clustering closely with the melanocyte progenitors identified in *casper* eyes.

(**G**) Schematic illustrating GNAQ^{Q209L}-driven uveal melanoma (UM) in the context of tumor suppressor loss. Melanocyte progenitor cells (*pax3a/b, tfec, sox4a*) can directly give rise to UM when oncogenic GNAQ^{Q209L} is present (black arrow), or differentiate into MITF^{high} melanocytes that preferentially form nevi (black arrow). These nevi may subsequently progress to UM following reduced MITF activity (gray dashed arrow). In contrast, germline *mitfa* loss blocks melanocyte differentiation and expands melanocyte progenitors, enabling GNAQ^{Q209L} to drive UM directly from this progenitor population.

977 1. Jager, M.J., Shields, C.L., Cebulla, C.M., Abdel-Rahman, M.H., Grossniklaus, H.E., Stern,
978 M.H., Carvajal, R.D., Belfort, R.N., Jia, R., Shields, J.A., and Damato, B.E. (2020). Uveal
979 melanoma. Nat Rev Dis Primers *6*, 24. 10.1038/s41572-020-0158-0.
980 2. Van Raamsdonk, C.D., Bezrookove, V., Green, G., Bauer, J., Gaugler, L., O'Brien, J.M.,
981 Simpson, E.M., Barsh, G.S., and Bastian, B.C. (2009). Frequent somatic mutations of
982 GNAQ in uveal melanoma and blue naevi. Nature *457*, 599-602. 10.1038/nature07586.
983 3. Kaliki, S., and Shields, C.L. (2017). Uveal melanoma: relatively rare but deadly cancer. Eye
984 (Lond) *31*, 241-257. 10.1038/eye.2016.275.
985 4. Yu, F.X., Luo, J., Mo, J.S., Liu, G., Kim, Y.C., Meng, Z., Zhao, L., Peyman, G., Ouyang, H.,
986 Jiang, W., et al. (2014). Mutant Gq/11 promote uveal melanoma tumorigenesis by
987 activating YAP. Cancer Cell *25*, 822-830. 10.1016/j.ccr.2014.04.017.
988 5. Phelps, G.B., Amsterdam, A., Hagen, H.R., García, N.Z., and Lees, J.A. (2022). MITF
989 deficiency and oncogenic GNAQ each promote proliferation programs in zebrafish
990 melanocyte lineage cells. Pigment Cell Melanoma Res *35*, 539-547. 10.1111/pcmr.13057.
991 6. Ceol, C.J., Houvras, Y., Jane-Valbuena, J., Bilodeau, S., Orlando, D.A., Battisti, V., Fritsch,
992 L., Lin, W.M., Hollmann, T.J., Ferré, F., et al. (2011). The histone methyltransferase
993 SETDB1 is recurrently amplified in melanoma and accelerates its onset. Nature *471*, 513-
994 517. 10.1038/nature09806.
995 7. Singh, A.P., Dinwiddie, A., Mahalwar, P., Schach, U., Linker, C., Irion, U., and Nüsslein-
996 Volhard, C. (2016). Pigment Cell Progenitors in Zebrafish Remain Multipotent through
997 Metamorphosis. Dev Cell *38*, 316-330. 10.1016/j.devcel.2016.06.020.
998 8. Callahan, S.J., Tepan, S., Zhang, Y.M., Lindsay, H., Burger, A., Campbell, N.R., Kim, I.S.,
999 Hollmann, T.J., Studer, L., Mosimann, C., and White, R.M. (2018). Cancer modeling by
1000 Transgene Electroporation in Adult Zebrafish (TEAZ). Dis Model Mech *11*.
1001 10.1242/dmm.034561.
1002 9. D'Agati, G., Beltre, R., Sessa, A., Burger, A., Zhou, Y., Mosimann, C., and White, R.M.
1003 (2017). A defect in the mitochondrial protein Mpv17 underlies the transparent casper
1004 zebrafish. Dev Biol *430*, 11-17. 10.1016/j.ydbio.2017.07.017.
1005 10. White, R.M., Sessa, A., Burke, C., Bowman, T., LeBlanc, J., Ceol, C., Bourque, C., Dovey,
1006 M., Goessling, W., Burns, C.E., and Zon, L.I. (2008). Transparent adult zebrafish as a tool
1007 for in vivo transplantation analysis. Cell Stem Cell *2*, 183-189.
1008 10.1016/j.stem.2007.11.002.
1009 11. Lister, J.A., Robertson, C.P., Lepage, T., Johnson, S.L., and Raible, D.W. (1999). nacre
1010 encodes a zebrafish microphthalmia-related protein that regulates neural-crest-derived
1011 pigment cell fate. Development *126*, 3757-3767. 10.1242/dev.126.17.3757.
1012 12. Butler, A., Hoffman, P., Smibert, P., Papalexi, E., and Satija, R. (2018). Integrating single-
1013 cell transcriptomic data across different conditions, technologies, and species. Nat
1014 Biotechnol *36*, 411-420. 10.1038/nbt.4096.
1015 13. Sur, A., Wang, Y., Capar, P., Margolin, G., Prochaska, M.K., and Farrell, J.A. (2023). Single-
1016 cell analysis of shared signatures and transcriptional diversity during zebrafish
1017 development. Dev Cell *58*, 3028-3047.e3012. 10.1016/j.devcel.2023.11.001.
1018 14. Voigt, A.P., Whitmore, S.S., Lessing, N.D., DeLuca, A.P., Tucker, B.A., Stone, E.M., Mullins,
1019 R.F., and Scheetz, T.E. (2020). Spectacle: An interactive resource for ocular single-cell
1020 RNA sequencing data analysis. Exp Eye Res *200*, 108204. 10.1016/j.exer.2020.108204.

1021 15. Kolberg, L., Raudvere, U., Kuzmin, I., Adler, P., Vilo, J., and Peterson, H. (2023). g:Profiler-
1022 interoperable web service for functional enrichment analysis and gene identifier
1023 mapping (2023 update). Nucleic Acids Res *51*, W207-w212. 10.1093/nar/gkad347.
1024 16. Krämer, A., Green, J., Pollard, J., Jr., and Tugendreich, S. (2014). Causal analysis
1025 approaches in Ingenuity Pathway Analysis. Bioinformatics *30*, 523-530.
1026 10.1093/bioinformatics/btt703.
1027 17. Subramanian, A., Tamayo, P., Mootha, V.K., Mukherjee, S., Ebert, B.L., Gillette, M.A.,
1028 Paulovich, A., Pomeroy, S.L., Golub, T.R., Lander, E.S., and Mesirov, J.P. (2005). Gene set
1029 enrichment analysis: a knowledge-based approach for interpreting genome-wide
1030 expression profiles. Proc Natl Acad Sci U S A *102*, 15545-15550.
1031 10.1073/pnas.0506580102.
1032 18. Trapnell, C., Cacchiarelli, D., Grimsby, J., Pokharel, P., Li, S., Morse, M., Lennon, N.J.,
1033 Livak, K.J., Mikkelsen, T.S., and Rinn, J.L. (2014). The dynamics and regulators of cell fate
1034 decisions are revealed by pseudotemporal ordering of single cells. Nat Biotechnol *32*,
1035 381-386. 10.1038/nbt.2859.
1036 19. Bloh, K., Kanchana, R., Bialk, P., Banas, K., Zhang, Z., Yoo, B.C., and Kmiec, E.B. (2021).
1037 Deconvolution of Complex DNA Repair (DECODR): Establishing a Novel Deconvolution
1038 Algorithm for Comprehensive Analysis of CRISPR-Edited Sanger Sequencing Data. Crispr j
1039 *4*, 120-131. 10.1089/crispr.2020.0022.
1040 20. Richardson, R., Tracey-White, D., Webster, A., and Moosajee, M. (2017). The zebrafish
1041 eye-a paradigm for investigating human ocular genetics. Eye (Lond) *31*, 68-86.
1042 10.1038/eye.2016.198.
1043 21. McMenamin, P.G., Shields, G.T., Seyed-Razavi, Y., Kalirai, H., Insall, R.H., Machesky, L.M.,
1044 and Coupland, S.E. (2020). Melanoblasts Populate the Mouse Choroid Earlier in
1045 Development Than Previously Described. Invest Ophthalmol Vis Sci *61*, 33.
1046 10.1167/iovs.61.10.33.
1047 22. Voigt, A.P., Mulfaul, K., Mullin, N.K., Flamme-Wiese, M.J., Giacalone, J.C., Stone, E.M.,
1048 Tucker, B.A., Scheetz, T.E., and Mullins, R.F. (2019). Single-cell transcriptomics of the
1049 human retinal pigment epithelium and choroid in health and macular degeneration. Proc
1050 Natl Acad Sci U S A *116*, 24100-24107. 10.1073/pnas.1914143116.
1051 23. Howe, D.G., Bradford, Y.M., Conlin, T., Eagle, A.E., Fashena, D., Frazer, K., Knight, J., Mani,
1052 P., Martin, R., Moxon, S.A., et al. (2013). ZFIN, the Zebrafish Model Organism Database:
1053 increased support for mutants and transgenics. Nucleic Acids Res *41*, D854-860.
1054 10.1093/nar/gks938.
1055 24. Tatarakis, D., Cang, Z., Wu, X., Sharma, P.P., Karikomi, M., MacLean, A.L., Nie, Q., and
1056 Schilling, T.F. (2021). Single-cell transcriptomic analysis of zebrafish cranial neural crest
1057 reveals spatiotemporal regulation of lineage decisions during development. Cell Rep *37*,
1058 110140. 10.1016/j.celrep.2021.110140.
1059 25. Simões-Costa, M., and Bronner, M.E. (2015). Establishing neural crest identity: a gene
1060 regulatory recipe. Development *142*, 242-257. 10.1242/dev.105445.
1061 26. Robertson, A.G., Shih, J., Yau, C., Gibb, E.A., Oba, J., Mungall, K.L., Hess, J.M.,
1062 Uzunangelov, V., Walter, V., Danilova, L., et al. (2017). Integrative Analysis Identifies Four
1063 Molecular and Clinical Subsets in Uveal Melanoma. Cancer Cell *32*, 204-220.e215.
1064 10.1016/j.ccell.2017.07.003.

1065 27. Hunter, M.V., Joshi, E., Bowker, S., Montal, E., Ma, Y., Kim, Y.H., Yang, Z., Tuffery, L., Li, Z.,
1066 Rosiek, E., et al. (2025). Mechanical confinement governs phenotypic plasticity in
1067 melanoma. Nature. 10.1038/s41586-025-09445-6.
1068 28. Hunter, M.V., Moncada, R., Weiss, J.M., Yanai, I., and White, R.M. (2021). Spatially
1069 resolved transcriptomics reveals the architecture of the tumor-microenvironment
1070 interface. Nat Commun *12*, 6278. 10.1038/s41467-021-26614-z.
1071 29. Liu, T., Zhou, L., Xiao, Y., Andl, T., and Zhang, Y. (2022). BRAF Inhibitors Reprogram
1072 Cancer-Associated Fibroblasts to Drive Matrix Remodeling and Therapeutic Escape in
1073 Melanoma. Cancer Res *82*, 419-432. 10.1158/0008-5472.Can-21-0614.
1074 30. Mao, X., Xu, J., Wang, W., Liang, C., Hua, J., Liu, J., Zhang, B., Meng, Q., Yu, X., and Shi, S.
1075 (2021). Crosstalk between cancer-associated fibroblasts and immune cells in the tumor
1076 microenvironment: new findings and future perspectives. Mol Cancer *20*, 131.
1077 10.1186/s12943-021-01428-1.
1078 31. Wang, J., Song, Y., Li, Z., Gao, T., Shen, W., Kang, Z., and Xu, C. (2025). Combining single-
1079 cell and bulk RNA sequencing to identify CAF-related signature for prognostic prediction
1080 and treatment response in patients with melanoma. Sci Rep *15*, 29082. 10.1038/s41598-
1081 025-14979-w.
1082 32. Jin, S., Guerrero-Juarez, C.F., Zhang, L., Chang, I., Ramos, R., Kuan, C.H., Myung, P., Plikus,
1083 M.V., and Nie, Q. (2021). Inference and analysis of cell-cell communication using
1084 CellChat. Nat Commun *12*, 1088. 10.1038/s41467-021-21246-9.
1085 33. Kaochar, S., Dong, J., Torres, M., Rajapakshe, K., Nikolos, F., Davis, C.M., Ehli, E.A., Coarfa,
1086 C., Mitsiades, N., and Poulaki, V. (2018). ICG-001 Exerts Potent Anticancer Activity
1087 Against Uveal Melanoma Cells. Invest Ophthalmol Vis Sci *59*, 132-143. 10.1167/iovs.17-
1088 22454.
1089 34. Zheng, L., Liu, Y., and Pan, J. (2017). Inhibitory effect of pyrvinium pamoate on uveal
1090 melanoma cells involves blocking of Wnt/β-catenin pathway. Acta Biochim Biophys Sin
1091 (Shanghai) *49*, 890-898. 10.1093/abbs/gmx089.
1092 35. Wu, S., Han, M., and Zhang, C. (2022). Overexpression of microRNA-130a represses
1093 uveal melanoma cell migration and invasion through inactivation of the Wnt/β-catenin
1094 signaling pathway by downregulating USP6. Cancer Gene Ther *29*, 930-939.
1095 10.1038/s41417-021-00377-7.
1096 36. Zuidervaart, W., van Nieuwpoort, F., Stark, M., Dijkman, R., Packer, L., Borgstein, A.M.,
1097 Pavey, S., van der Velden, P., Out, C., Jager, M.J., et al. (2005). Activation of the MAPK
1098 pathway is a common event in uveal melanomas although it rarely occurs through
1099 mutation of BRAF or RAS. Br J Cancer *92*, 2032-2038. 10.1038/sj.bjc.6602598.
1100 37. Chen, X., Wu, Q., Depeille, P., Chen, P., Thornton, S., Kalirai, H., Coupland, S.E., Roose,
1101 J.P., and Bastian, B.C. (2017). RasGRP3 Mediates MAPK Pathway Activation in GNAQ
1102 Mutant Uveal Melanoma. Cancer Cell *31*, 685-696.e686. 10.1016/j.ccell.2017.04.002.
1103 38. Rimoldi, D., Salvi, S., Liénard, D., Lejeune, F.J., Speiser, D., Zografos, L., and Cerottini, J.C.
1104 (2003). Lack of BRAF mutations in uveal melanoma. Cancer Res *63*, 5712-5715.
1105 39. Abdel-Rahman, M.H., Yang, Y., Zhou, X.P., Craig, E.L., Davidorf, F.H., and Eng, C. (2006).
1106 High frequency of submicroscopic hemizygous deletion is a major mechanism of loss of
1107 expression of PTEN in uveal melanoma. J Clin Oncol *24*, 288-295.
1108 10.1200/jco.2005.02.2418.

1109 40. Pópulo, H., Soares, P., Rocha, A.S., Silva, P., and Lopes, J.M. (2010). Evaluation of the
1110 mTOR pathway in ocular (uvea and conjunctiva) melanoma. Melanoma Res *20*, 107-117.
1111 10.1097/CMR.0b013e32832ccd09.
1112 41. Woodman, S.E. (2012). Metastatic uveal melanoma: biology and emerging treatments.
1113 Cancer J *18*, 148-152. 10.1097/PPO.0b013e31824bd256.
1114 42. Petratou, K., Spencer, S.A., Kelsh, R.N., and Lister, J.A. (2021). The MITF paralog tfec is
1115 required in neural crest development for fate specification of the iridophore lineage
1116 from a multipotent pigment cell progenitor. PLoS One *16*, e0244794.
1117 10.1371/journal.pone.0244794.
1118 43. Kenny, C., Dilshat, R., Seberg, H.E., Van Otterloo, E., Bonde, G., Helverson, A., Franke,
1119 C.M., Steingrímsson, E., and Cornell, R.A. (2022). TFAP2 paralogs facilitate chromatin
1120 access for MITF at pigmentation and cell proliferation genes. PLoS Genet *18*, e1010207.
1121 10.1371/journal.pgen.1010207.
1122 44. Ulrich, E., Kistenmacher, S., Martin, G., Schlötzer-Schrehardt, U., Seitz, B., Auw-Hädrich,
1123 C., Schlunck, G., Reinhard, T., and Polisetti, N. (2025). PAX3 expression patterns in ocular
1124 surface melanocytes. Sci Rep *15*, 12472. 10.1038/s41598-025-90318-3.
1125 45. Kumar, N., Singh, M.K., Singh, L., Jha, J., Pushker, N., Lomi, N., Meel, R., Sen, S., and
1126 Kashyap, S. (2025). Prognostic significance of pigmentation and stem cell markers in
1127 Indian population of uveal melanoma. Br J Ophthalmol *109*, 799-808. 10.1136/bjo-2024-
1128 325886.
1129 46. Lumaquin-Yin, D., Montal, E., Johns, E., Baggiolini, A., Huang, T.H., Ma, Y., LaPlante, C.,
1130 Suresh, S., Studer, L., and White, R.M. (2023). Lipid droplets are a metabolic vulnerability
1131 in melanoma. Nat Commun *14*, 3192. 10.1038/s41467-023-38831-9.
1132 47. Baggiolini, A., Callahan, S.J., Montal, E., Weiss, J.M., Trieu, T., Tagore, M.M., Tischfield,
1133 S.E., Walsh, R.M., Suresh, S., Fan, Y., et al. (2021). Developmental chromatin programs
1134 determine oncogenic competence in melanoma. Science *373*, eabc1048.
1135 10.1126/science.abc1048.
1136 48. Brombin, A., Simpson, D.J., Travnickova, J., Brunsdon, H., Zeng, Z., Lu, Y., Young, A.I.J.,
1137 Chandra, T., and Patton, E.E. (2022). Tfap2b specifies an embryonic melanocyte stem cell
1138 that retains adult multifate potential. Cell Rep *38*, 110234.
1139 10.1016/j.celrep.2021.110234.
1140 49. Kubic, J.D., Young, K.P., Plummer, R.S., Ludvik, A.E., and Lang, D. (2008). Pigmentation
1141 PAX-ways: the role of Pax3 in melanogenesis, melanocyte stem cell maintenance, and
1142 disease. Pigment Cell Melanoma Res *21*, 627-645. 10.1111/j.1755-148X.2008.00514.x.
1143 50. Dutton, K.A., Pauliny, A., Lopes, S.S., Elworthy, S., Carney, T.J., Rauch, J., Geisler, R.,
1144 Haffter, P., and Kelsh, R.N. (2001). Zebrafish colourless encodes sox10 and specifies non-
1145 ectomesenchymal neural crest fates. Development *128*, 4113-4125.
1146 10.1242/dev.128.21.4113.
1147 51. Brombin, A., MacMaster, S., Travnickova, J., Wyatt, C., Brunsdon, H., Ramsey, E., Vu, H.N.,
1148 Steingrimsson, E., Chandra, T., and Patton, E.E. (2025). Loss of MITF activity leads to
1149 emergent cell states from the melanocyte stem cell lineage. bioRxiv,
1150 2025.2012.2023.695681. 10.64898/2025.12.23.695681.

1151 52. Frantz, W.T., Iyengar, S., Neiswender, J., Cousineau, A., Maehr, R., and Ceol, C.J. (2023).
1152 Pigment cell progenitor heterogeneity and reiteration of developmental signaling
1153 underlie melanocyte regeneration in zebrafish. Elife *12*. 10.7554/eLife.78942.
1154 53. Thomas, A.J., and Erickson, C.A. (2009). FOXD3 regulates the lineage switch between
1155 neural crest-derived glial cells and pigment cells by repressing MITF through a non-
1156 canonical mechanism. Development *136*, 1849-1858. 10.1242/dev.031989.
1157 54. Youkilis, J.C., and Bassnett, S. (2021). Single-cell RNA-sequencing analysis of the ciliary
1158 epithelium and contiguous tissues in the mouse eye. Exp Eye Res *213*, 108811.
1159 10.1016/j.exer.2021.108811.
1160 55. Lang, D., Lu, M.M., Huang, L., Engleka, K.A., Zhang, M., Chu, E.Y., Lipner, S., Skoultchi, A.,
1161 Millar, S.E., and Epstein, J.A. (2005). Pax3 functions at a nodal point in melanocyte stem
1162 cell differentiation. Nature *433*, 884-887. 10.1038/nature03292.
1163 56. Johns, E., Ma, Y., Louphrasitthiphol, P., Peralta, C., Hunter, M.V., Raymond, J.H., Molina,
1164 H., Goding, C.R., and White, R.M. (2025). The Lipid Droplet Protein DHRS3 Is a Regulator
1165 of Melanoma Cell State. Pigment Cell Melanoma Res *38*, e13208. 10.1111/pcmr.13208.
1166 57. Xu, Y., Xu, W.H., Yang, X.L., Zhang, H.L., and Zhang, X.F. (2020). Fatty acid-binding protein
1167 5 predicts poor prognosis in patients with uveal melanoma. Oncol Lett *19*, 1771-1780.
1168 10.3892/ol.2020.11301.
1169 58. Van Ly, D., Wang, D., Conway, R.M., Giblin, M., Liang, S., Lukeis, R., Lim, L.A., Hesson, L.,
1170 and Cherepanoff, S. (2020). Lipid-Producing Ciliochoroidal Melanoma with Expression of
1171 HMG-CoA Reductase. Ocul Oncol Pathol *6*, 416-421. 10.1159/000510393.
1172 59. Yavuzyigitoglu, S., Kilic, E., Vaarwater, J., de Klein, A., Paridaens, D., and Verdijk, R.M.
1173 (2016). Lipomatous Change in Uveal Melanoma: Histopathological,
1174 Immunohistochemical and Cytogenetic Analysis. Ocul Oncol Pathol *2*, 133-135.
1175 10.1159/000440981.
1176 60. Fiorentzis, M., Kalirai, H., Katopodis, P., and Coupland, S.E. (2017). Adipophilin
1177 expression in primary and metastatic uveal melanoma: a pilot study. Graefes Arch Clin
1178 Exp Ophthalmol *255*, 1049-1051. 10.1007/s00417-017-3630-0.
1179 61. Horvathova Kajabova, V., Soltysova, A., Demkova, L., Plesnikova, P., Lyskova, D., Furdova,
1180 A., Babal, P., and Smolkova, B. (2021). KIT Expression Is Regulated by DNA Methylation in
1181 Uveal Melanoma Tumors. Int J Mol Sci *22*. 10.3390/ijms221910748.
1182 62. Surriga, O., Rajasekhar, V.K., Ambrosini, G., Dogan, Y., Huang, R., and Schwartz, G.K.
1183 (2013). Crizotinib, a c-Met inhibitor, prevents metastasis in a metastatic uveal melanoma
1184 model. Mol Cancer Ther *12*, 2817-2826. 10.1158/1535-7163.Mct-13-0499.
1185 63. Cheng, H., Terai, M., Kageyama, K., Ozaki, S., McCue, P.A., Sato, T., and Aplin, A.E. (2015).
1186 Paracrine Effect of NRG1 and HGF Drives Resistance to MEK Inhibitors in Metastatic
1187 Uveal Melanoma. Cancer Res *75*, 2737-2748. 10.1158/0008-5472.Can-15-0370.
1188 64. Mitra, A.K., Sawada, K., Tiwari, P., Mui, K., Gwin, K., and Lengyel, E. (2011). Ligand-
1189 independent activation of c-Met by fibronectin and α(5)β(1)-integrin regulates ovarian
1190 cancer invasion and metastasis. Oncogene *30*, 1566-1576. 10.1038/onc.2010.532.
1191 65. Travnickova, J., Wojciechowska, S., Khamseh, A., Gautier, P., Brown, D.V., Lefevre, T.,
1192 Brombin, A., Ewing, A., Capper, A., Spitzer, M., et al. (2019). Zebrafish MITF-Low
1193 Melanoma Subtype Models Reveal Transcriptional Subclusters and MITF-Independent
1194 Residual Disease. Cancer Res *79*, 5769-5784. 10.1158/0008-5472.Can-19-0037.

1195 66. Lister, J.A., Lane, B.M., Nguyen, A., and Lunney, K. (2011). Embryonic expression of
1196 zebrafish MiT family genes tfe3b, tfeb, and tfec. Dev Dyn *240*, 2529-2538.
1197 10.1002/dvdy.22743.
1198 67. Chang, J., Campbell-Hanson, K.R., Vanneste, M., Bartschat, N.I., Nagel, R., Arnadottir,
1199 A.K., Vu, H.N., Montgomery, C., Yevdash, J., Jiang, J., et al. (2025). Antagonistic roles for
1200 MITF and TFE3 in melanoma plasticity. Cell Rep *44*, 115474.
1201 10.1016/j.celrep.2025.115474.
1202 68. Xu, X., Liu, X., Jarajapu, V., Neelature Sriramareddy, S., Konecny, F., Posorske, B., Dollar,
1203 J.J., Liu, X., Jasani, N., Wang, K., et al. (2026). A Multi-Step Immune-Competent
1204 Genetically Engineered Mouse Model Reveals Phenotypic Plasticity in Uveal Melanoma.
1205 Cancer Res. 10.1158/0008-5472.Can-25-2684.
1206 69. Hajkova, N., Hojny, J., Nemejcova, K., Dundr, P., Ulrych, J., Jirsova, K., Glezgova, J., and
1207 Ticha, I. (2018). Germline mutation in the TP53 gene in uveal melanoma. Sci Rep *8*, 7618.
1208 10.1038/s41598-018-26040-0.
1209 70. Harbour, J.W., Onken, M.D., Roberson, E.D., Duan, S., Cao, L., Worley, L.A., Council, M.L.,
1210 Matatall, K.A., Helms, C., and Bowcock, A.M. (2010). Frequent mutation of BAP1 in
1211 metastasizing uveal melanomas. Science *330*, 1410-1413. 10.1126/science.1194472.
1212 71. Brantley, M.A., Jr., and Harbour, J.W. (2000). Deregulation of the Rb and p53 pathways in
1213 uveal melanoma. Am J Pathol *157*, 1795-1801. 10.1016/s0002-9440(10)64817-1.
1214 72. Coupland, S.E., Anastassiou, G., Stang, A., Schilling, H., Anagnostopoulos, I., Bornfeld, N.,
1215 and Stein, H. (2000). The prognostic value of cyclin D1, p53, and MDM2 protein
1216 expression in uveal melanoma. J Pathol *191*, 120-126. 10.1002/(sici)1096-
1217 9896(200006)191:2<120::Aid-path591>3.0.Co;2-p.
1218 73. Paraoan, L., Gray, D., Hiscott, P., Ebrahimi, B., Damato, B., and Grierson, I. (2006).
1219 Expression of p53-induced apoptosis effector PERP in primary uveal melanomas:
1220 downregulation is associated with aggressive type. Exp Eye Res *83*, 911-919.
1221 10.1016/j.exer.2006.04.016.
1222 74. Davies, L., Spiller, D., White, M.R., Grierson, I., and Paraoan, L. (2011). PERP expression
1223 stabilizes active p53 via modulation of p53-MDM2 interaction in uveal melanoma cells.
1224 Cell Death Dis *2*, e136. 10.1038/cddis.2011.19.
1225 75. de Lange, J., Ly, L.V., Lodder, K., Verlaan-de Vries, M., Teunisse, A.F., Jager, M.J., and
1226 Jochemsen, A.G. (2012). Synergistic growth inhibition based on small-molecule p53
1227 activation as treatment for intraocular melanoma. Oncogene *31*, 1105-1116.
1228 10.1038/onc.2011.309.
1229

FIGURE 1

A

Strategy A

mitfa | GNAQ^{Q209L}-T2A-GFP | Cas9/CRISPR | mitfa

U6:gRNA (*tp53, ptena, ptenb* or non-targeting)

Strategy B

mitfa | GNAQ^{Q209L} | eGFP | mitfa

mitfa | Cas9/CRISPR

U6 | gRNA1 | U6 | gRNA2 | U6 | gRNA3

(*tp53, ptena, ptenb*)

B

Transgene Electroporation of Adult Zebrafish Skin (TEAZ-Skin)

Zebrafish lines

Wild-type (*AB*)

mitfa$^{w2/w2}$ (*nacre*)

mitfa$^{w2/w2}$: *mpv17*$^{a9/a9}$ (*casper*)

Cutaneous targeted injection of DNA

Electroporation

C

TEAZ-Skin (*Strategy B*)

Wild-type

Week 4

Week 8

Week 12

GFP

casper

Week 2

Week 4

Week 6

GFP

D

TEAZ-Skin (*Strategy B*)

Tumor free survival

Days

WT

Nacre

Casper

****

****

ns

TEAZ-Skin (GNAQ^{Q209L}: GFP)

GNAQ: GFP (WT)

GNAQ: GFP (Nacre)

GNAQ: GFP (Casper)

*

*

E

Sclera

Choroid

Vitreous

RPE

Cornea

Lens

Zonules

Ciliary Zone

Optic Nerve

Annular Ligament

Retina

Zebrafish

VIT

GCL

IPL

INL

ONL

POS

RPE

CH

SCL

Human

F

Choroid

Tg(mitfa:GFP)

DAPI GFP

Tg(mitfa:GFP)

Secondary only

DAPI GFP

Secondary only

G

Transgene Electroporation of Adult Zebrafish Eye (TEAZ-Eye)

Choroidal targeted injection

Electroporation

J

TEAZ-Eye (*Strategy B*)

Tumor free survival

Days

WT

Casper

**

H

Wild-type (*Strategy B*)

14 dpe

GFP

21 dpe

28 dpe

35 dpe

42 dpe

I

Casper (*Strategy B*)

14 dpe

GFP

21 dpe

28 dpe

H'

Wild-type (*Strategy B*)

180 dpe

I'

Casper (*Strategy B*)

met

40 dpe

K

Sclera

Uveal Melanoma

K'

DAPI GFP

Choroid

RPE

Retina

Lens

Cornea

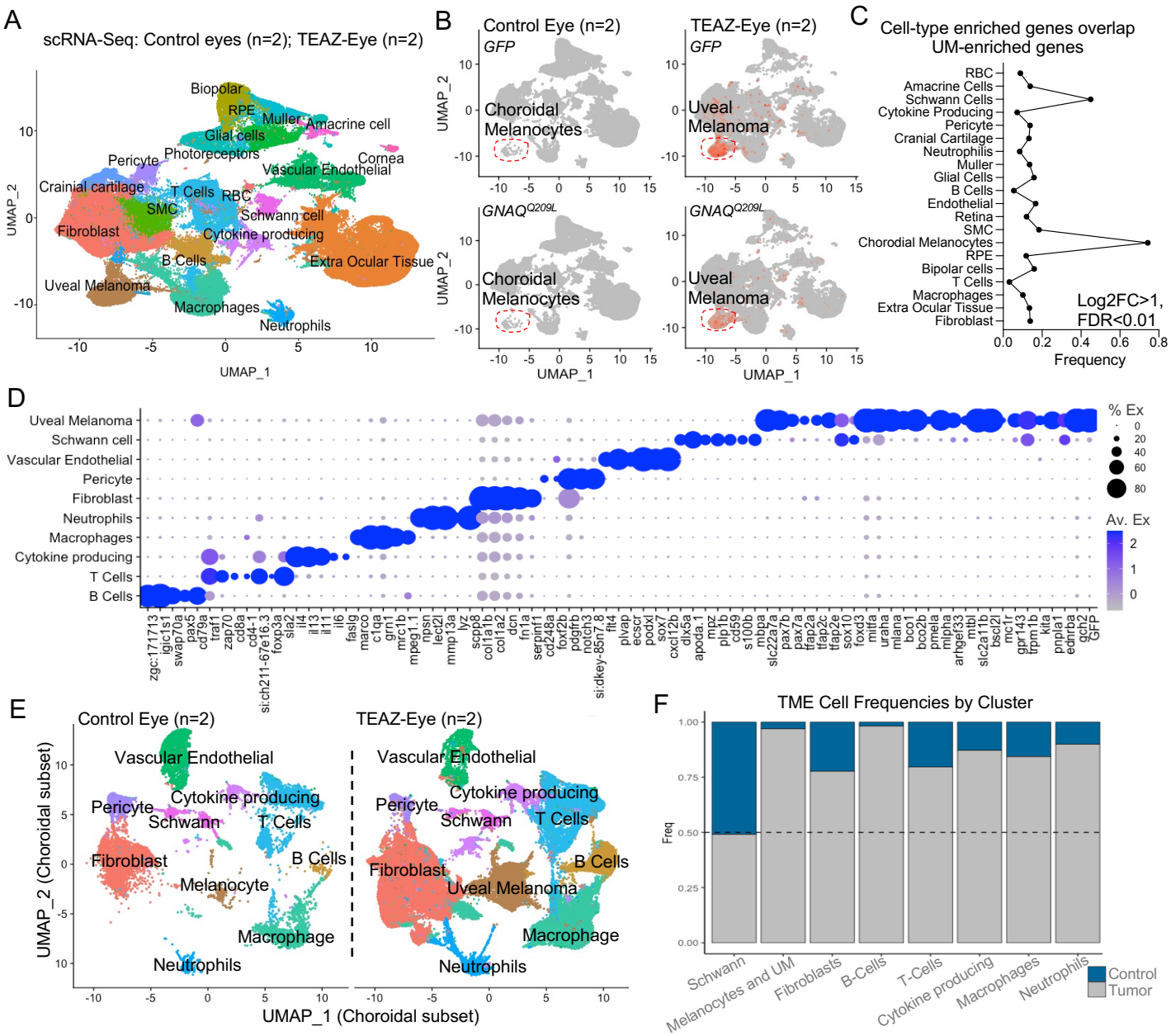
A
scRNA-Seq: Control eyes (n=2); TEAZ-Eye (n=2)
Biopolar
RPE
Muller
Amacrine cell
Glial cells
Photoreceptors
Pericyte
Cornea
Vascular Endothelial
Crainial cartilage
T Cells
RBC
SMC
Schwann cell
Fibroblast
Cytokine producing
B Cells
Extra Ocular Tissue
Uveal Melanoma
Macrophages
Neutrophils
UMAP_1
UMAP_2
B
Control Eye (n=2)
TEAZ-Eye (n=2)
GFP
Choroidal Melanocytes
Uveal Melanoma
GNAQQ209L
C
Cell-type enriched genes overlap UM-enriched genes
RBC
Amacrine Cells
Schwann Cells
Cytokine Producing
Pericyte
Cranial Cartilage
Neutrophilis
Muller
Glial Cells
B Cells
Endothelial
Retina
SMC
Chorodial Melanocytes
RPE
Bipolar cells
T Cells
Macrophages
Extra Ocular Tissue
Fibroblast
Log2FC>1, FDR<0.01
Frequency
D
Uveal Melanoma
Schwann cell
Vascular Endothelial
Pericyte
Fibroblast
Neutrophils
Macrophages
Cytokine producing
T Cells
B Cells
% Ex
Av. Ex
E
Control Eye (n=2)
TEAZ-Eye (n=2)
Vascular Endothelial
Cytokine producing
Pericyte
Schwann
T Cells
Fibroblast
B Cells
Melanocyte
Uveal Melanoma
Macrophage
Neutrophils
UMAP_2 (Choroidal subset)
UMAP_1 (Choroidal subset)
F
TME Cell Frequencies by Cluster
Freq
Schwann
Melanocytes and UM
Fibroblasts
B-Cells
T-Cells
Cytokine producing
Macrophages
Neutrophils
Control
Tumor
G
Log2FC>1, FDR<0.01
UM vs. TME
Choroidal Melanocytes vs. ME
1177
644
229
pax3a/b
tfap2e
fabp3
igals2a
pmela
myca/b
met
ednrb
bscl2l
gch2
kita
mlpha
sox10
foxd3
mlana
mitfa
pax7b
thy1
G'
Known motifs
MiT/TFE, 1e-13, rank 1
de novo motifs
PAX3/7, HOXB13 , 1e-12, rank 1
H
Choroidal Melanocytes vs. UM
fabp3
iah1
zgc:162150
thy1
bscl2l
gch2
lgals2a
pax7b
dgat2
mlpha
sox10
foxd3
kita
ednrba
% Ex
Av. Ex
TME
Choroidal Melanocytes
UM
L
Normal Fibroblasts (NF) vs. CAFs
ECM
fn1a
fnbp1l
lamtor3
fnta
lamtor2
mmp15a
fn1b
postna
lamc2
ECM regulators
mmp9
lman1
anxa5b
anxa2a
lgals2a
ctps1a
serpinb1l1
serpine2
ctsz
ctsk
serpinh1a
ctsa
ctsba
cst14b.1
ctsh
ctsd
serpine1
TNFs
tnfaip6
il34
ilf2
tnfb
tgfb1b
il11
lamb1b
Collagens
col5a3a
col5a2a
col5a1
col4a5
col21a1
col18a1a
col15a1a
col12a1a
% EX
Av. Ex
TME
NF
CAF
I
Disease Free Survival
Low KIT Group
High KIT Group
Logrank p=0.00036
HR(high)=6
p(HR)=0.0016
n(high)=39
n(low)=39
Percent survival
Months
KIT
UM
J
Disease Free Survival
Low FABP3 Group
High FABP3 Group
Logrank p=0.0033
HR(high)=4.1
p(HR)=0.0067
n(high)=39
n(low)=39
FABP3
UM
K
Overall Survival
Low LGALS2 Group
High LGALS2 Group
Logrank p=6.3e-05
HR(high)=8.9
p(HR)=0.00069
n(high)=39
n(low)=39
LGALS2
UM

FIGURE 3

A Control eye (n=3); Control skin (n=2); TEAZ-Eye (n=2), TEAZ-Skin (n=2)

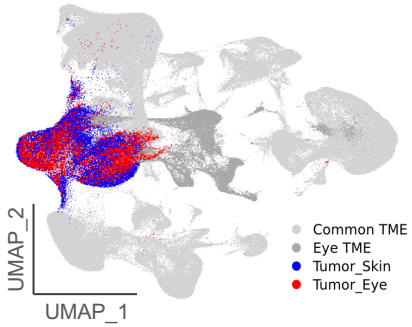

B Comparison of Primary Melanocytes and GNAQ-induced Melanoma Across Eye and Skin

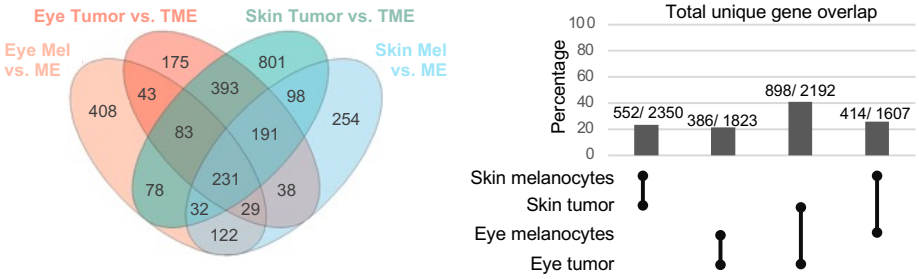

C DEGs: Primary Melanocytes Eye vs. Skin (FDR<0.01, Log2FC >|0.5|)

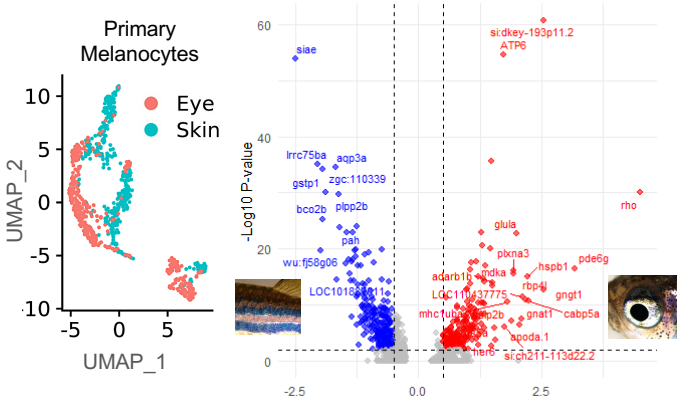

E DEGs: GNAQ-induced Melanoma Eye vs. Skin (FDR<0.01, Log2FC >|0.5|)

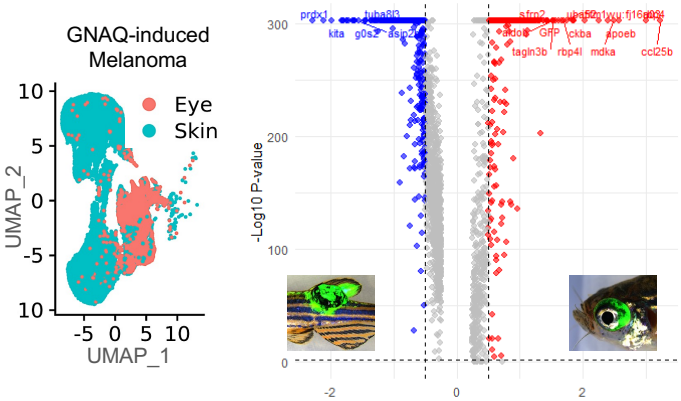

D

Up in Skin Melanocytes

DNA Repair

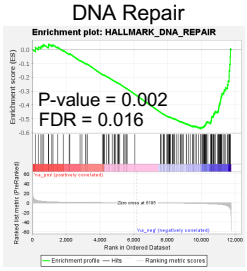

UV Response Up

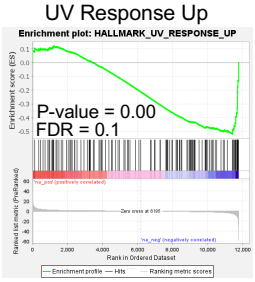

Up in Eye Melanocytes

Oxidative phosphorylation

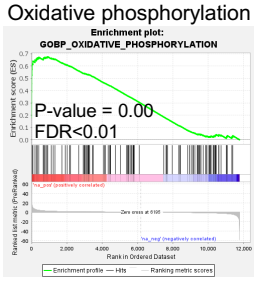

UV Response Down

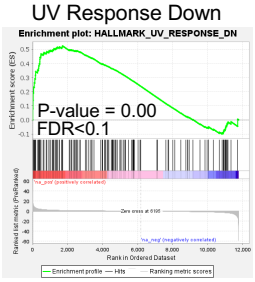

F

Up in Skin Melanoma

PI3K/AKT/MTOR

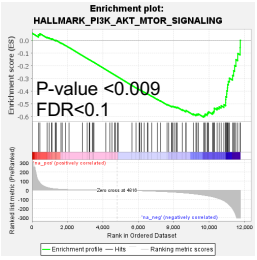

RHO GTPase

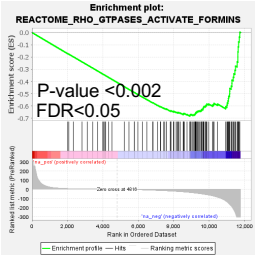

YAP1 activity

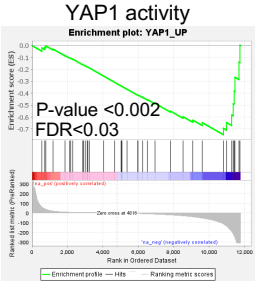

Up in Eye Melanoma

EMT transition

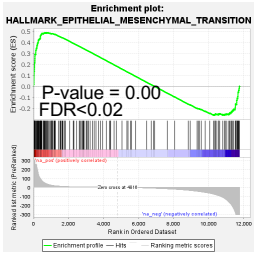

Selenoamino acid metabolism

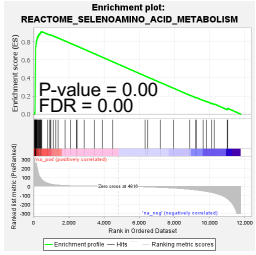

FIGURE 4

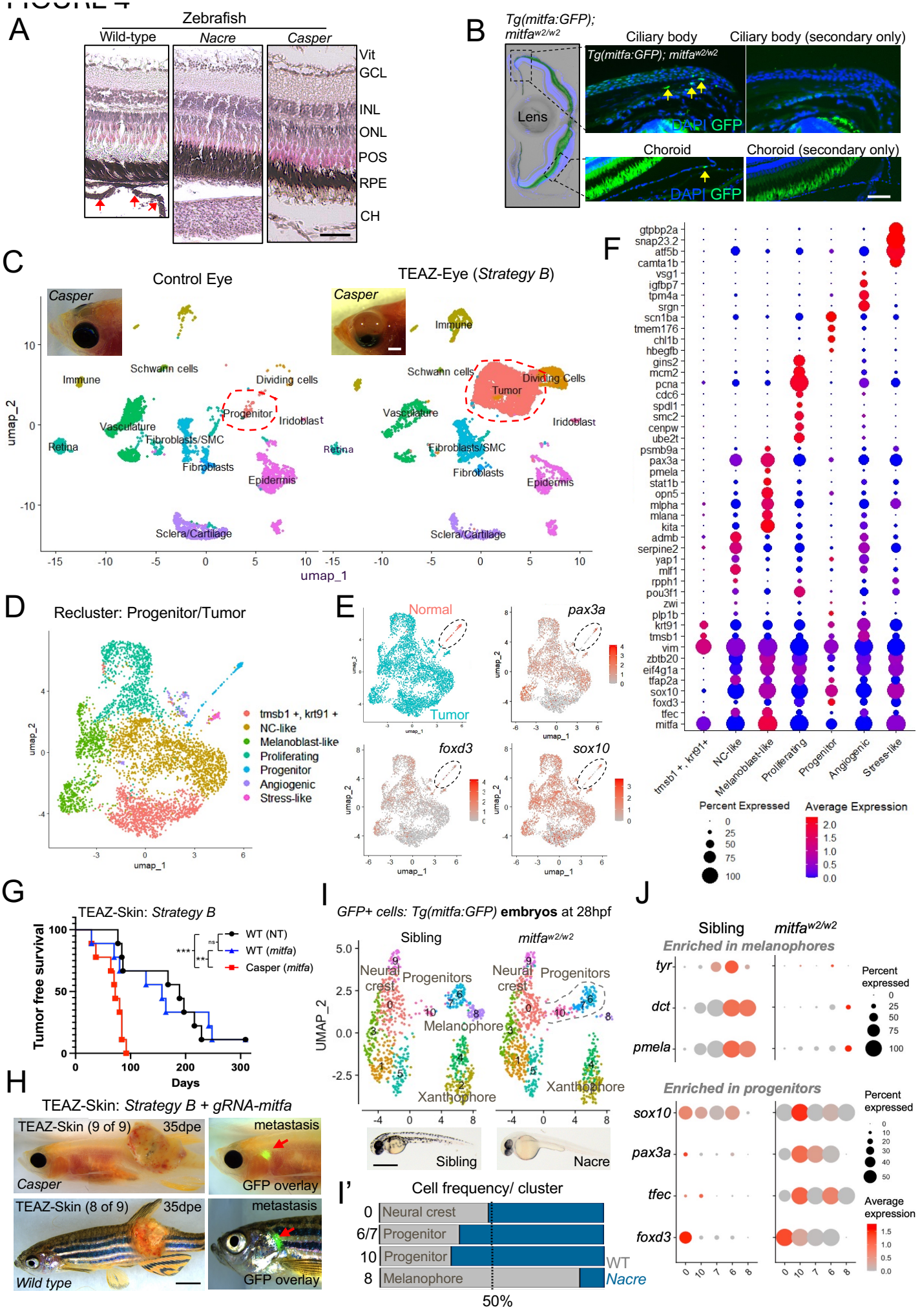
A
Zebrafish
Wild-type
Nacre
Casper
Vit
GCL
INL
ONL
POS
RPE
CH
B
Tg(mitfa:GFP); mitfa w2/w2
Lens
Ciliary body
Ciliary body (secondary only)
Tg(mitfa:GFP); mitfa w2/w2
DAPI GFP
Choroid
Choroid (secondary only)
DAPI GFP
C
Control Eye
TEAZ-Eye (Strategy B)
Casper
Immune
Schwann cells
Dividing cells
Tumor
Dividing Cells
Progenitor
Iridoblast
Vasculature
Fibroblasts/SMC
Retina
Fibroblasts
Epidermis
Sclera/Cartilage
umap_2
umap_1
D
Recluster: Progenitor/Tumor
tmsb1 +, krt91 +
NC-like
Melanoblast-like
Proliferating
Progenitor
Angiogenic
Stress-like
umap_2
umap_1
E
Normal
Tumor
pax3a
foxd3
sox10
umap_1
umap_2
F
gtpbp2a
snap23.2
atf5b
camta1b
vsg1
igfbp7
tpm4a
srgn
scn1ba
tmem176
chl1b
hbegfb
gins2
mcm2
pcna
cdc6
spdl1
smc2
cenpw
ube2t
psmb9a
pax3a
pmela
stat1b
opn5
mlpha
mlana
kita
admb
serpine2
yap1
mlf1
rpph1
pou3f1
zwi
plp1b
krt91
tmsb1
vim
zbtb20
eif4g1a
tfap2a
sox10
foxd3
tfec
mitfa
tmsb1 +, krt91+
NC-like
Melanoblast-like
Proliferating
Progenitor
Angiogenic
Stress-like
Percent Expressed
Average Expression
G
TEAZ-Skin: Strategy B
Tumor free survival
Days
WT (NT)
WT (mitfa)
Casper (mitfa)
H
TEAZ-Skin: Strategy B + gRNA-mitfa
TEAZ-Skin (9 of 9)
35dpe
metastasis
Casper
GFP overlay
TEAZ-Skin (8 of 9)
35dpe
metastasis
Wild type
GFP overlay
I
GFP+ cells: Tg(mitfa:GFP) embryos at 28hpf
Sibling
mitfa w2/w2
Neural crest
Progenitors
Melanophore
Xanthophore
UMAP_2
Sibling
Nacre
I'
Cell frequency/ cluster
Neural crest
Progenitor
Progenitor
Melanophore
WT
Nacre
50%
J
Sibling
mitfa w2/w2
Enriched in melanophores
tyr
dct
pmela
Percent expressed
Enriched in progenitors
sox10
pax3a
tfec
foxd3
Percent expressed
Average expression

FIGURE 5

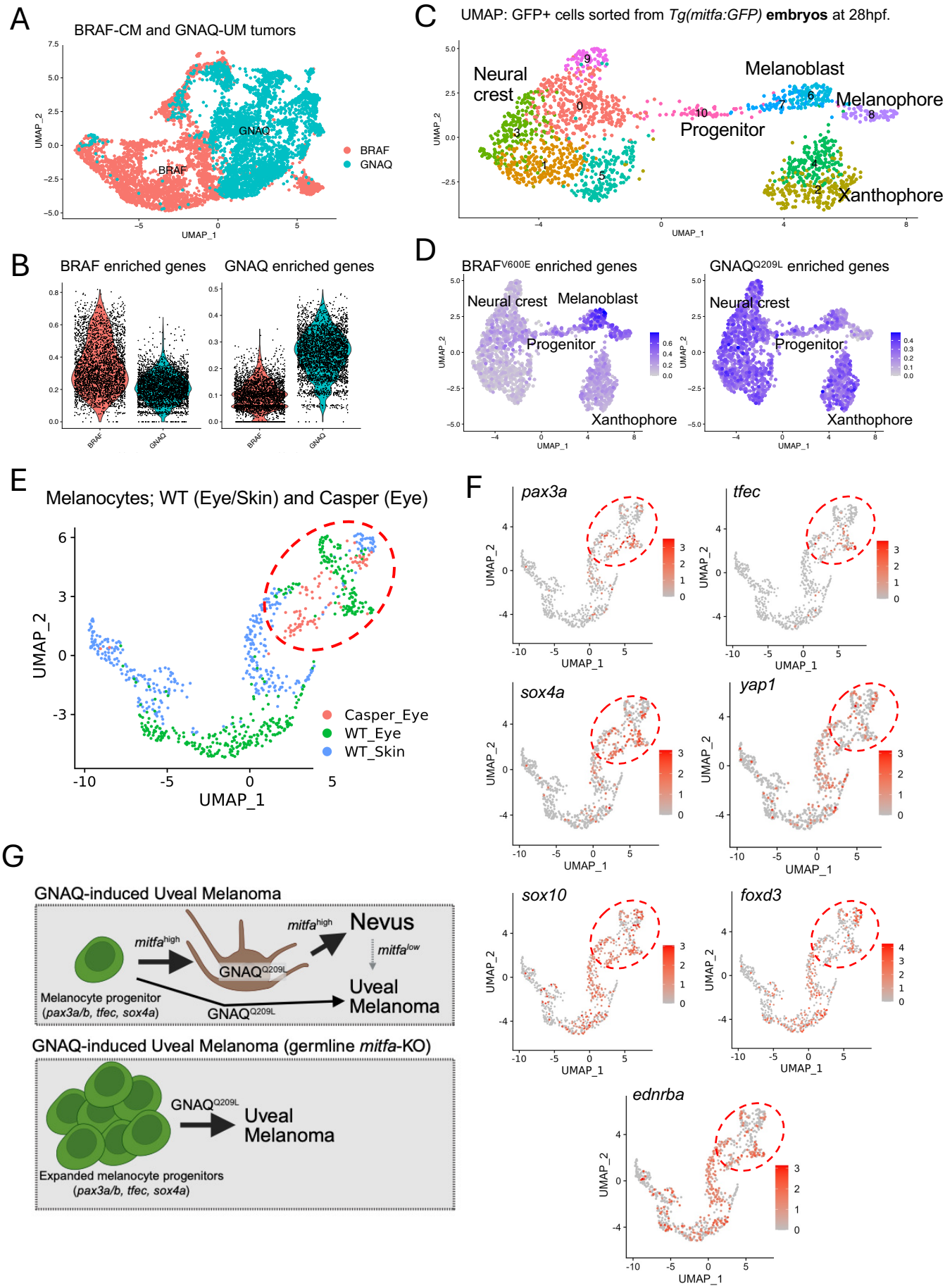
A
BRAF-CM and GNAQ-UM tumors
BRAF
GNAQ
UMAP_1
UMAP_2
C
UMAP: GFP+ cells sorted from Tg(mitfa:GFP) embryos at 28hpf.
Neural crest
Melanoblast
Melanophore
Progenitor
Xanthophore
B
BRAF enriched genes
GNAQ enriched genes
D
BRAFV600E enriched genes
GNAQQ209L enriched genes
Neural crest
Melanoblast
Progenitor
Xanthophore
E
Melanocytes; WT (Eye/Skin) and Casper (Eye)
Casper_Eye
WT_Eye
WT_Skin
F
pax3a
tfec
sox4a
yap1
sox10
foxd3
ednrba
G
GNAQ-induced Uveal Melanoma
mitfahigh
Nevus
mitfalow
GNAQQ209L
Uveal Melanoma
Melanocyte progenitor
(pax3a/b, tfec, sox4a)
GNAQ-induced Uveal Melanoma (germline mitfa-KO)
Expanded melanocyte progenitors
(pax3a/b, tfec, sox4a)

FIGURE S1

A

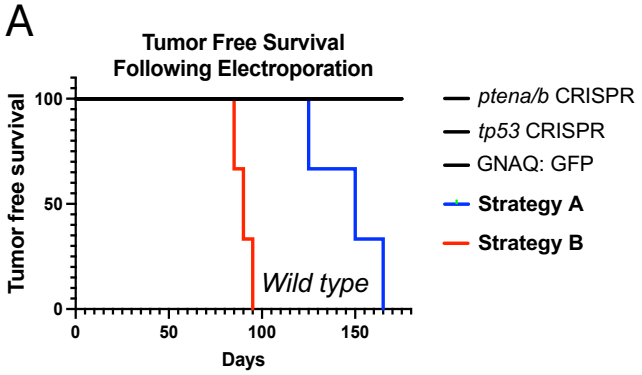

B

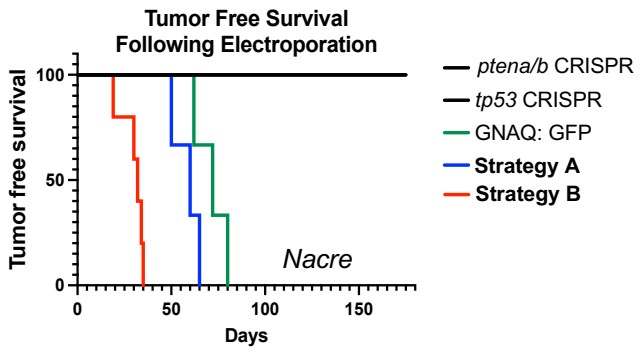

B'

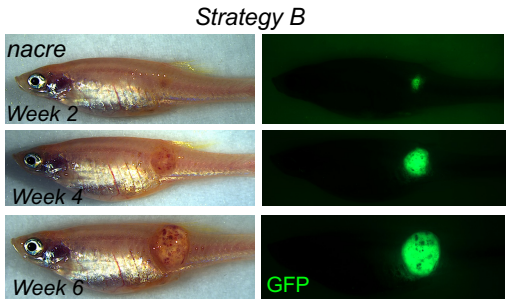

C

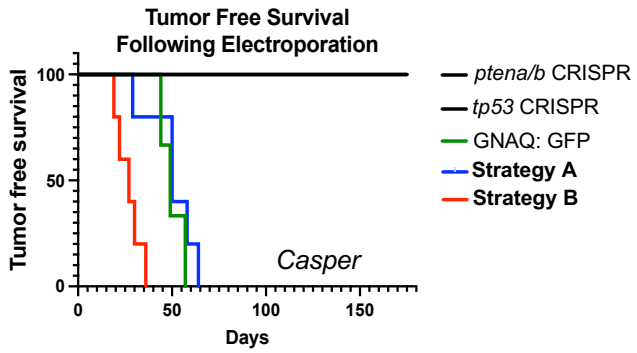

D

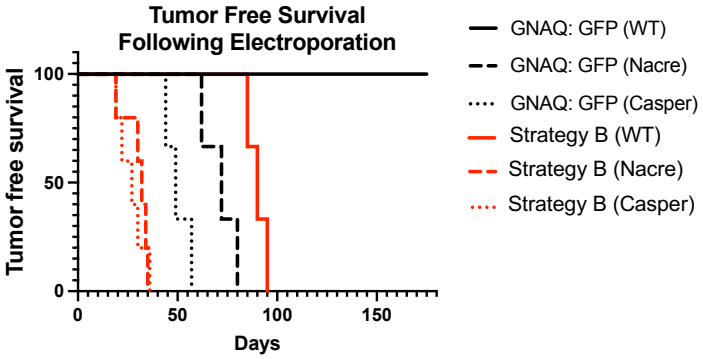

E

TEAZ-Skin in wild-type

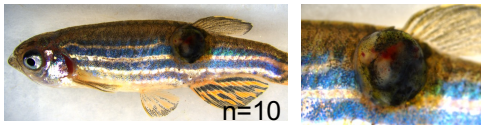

TEAZ-Skin in *casper*

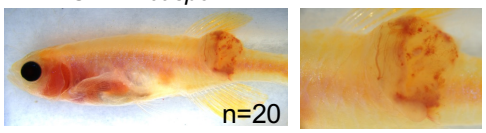

Xanthoma in *Tg*(*mitfa*:*BRAF*^{V600E}); *mitfa*$^{w2/w2}$; *tp53*$^{-/-}$)

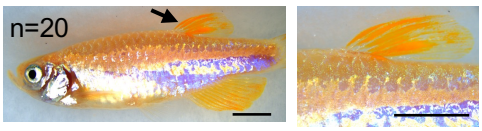

FIGURE S2

Tumor #	ptena	ptenb	tp53	# of edited genes
1				**3**
2				**3**
3				**2**
4				**3**
5				**3**
6				**3**
7				**3**
8				**3**
9				**3**
10				**3**
11				**3**
Germline	**ptena**	**ptenb**	**tp53**	
WT1				**0**
WT2				**0**

CRISPR editing

No editing

FIGURE S3

A

Tg(mitfa-GFP) Zebrafish Line

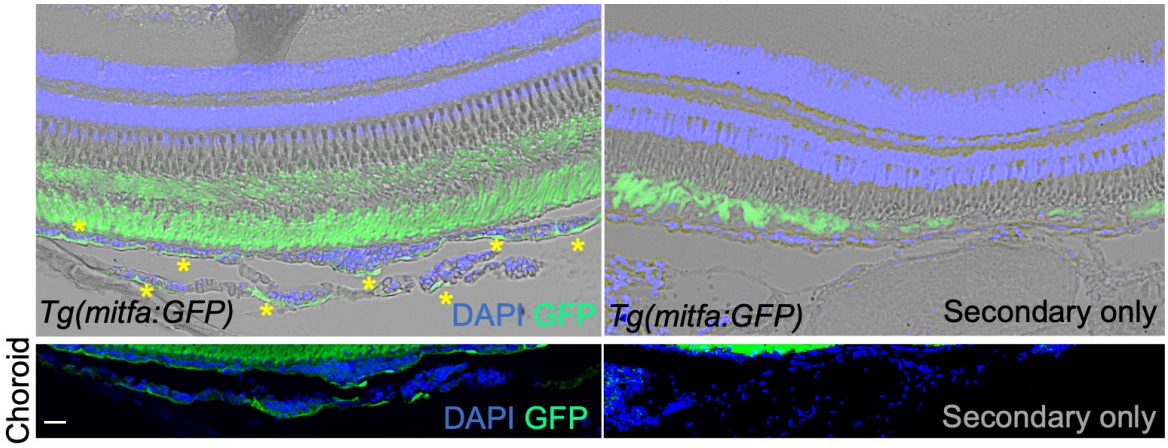

B

Tg(mitfa-GFP) Zebrafish Line

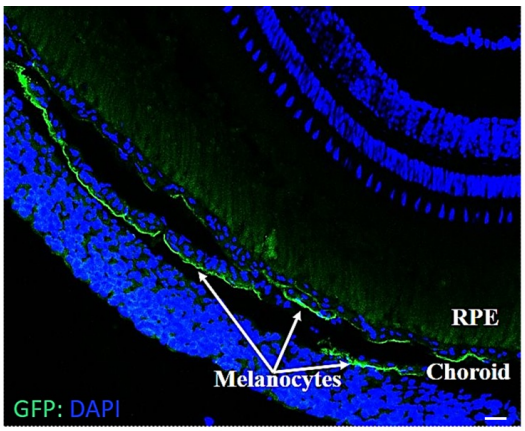

Anti-GFP IF

C

TEAZ-Eye using *mitfa:GFP* plasmids into WT Zebrafish

Choroid

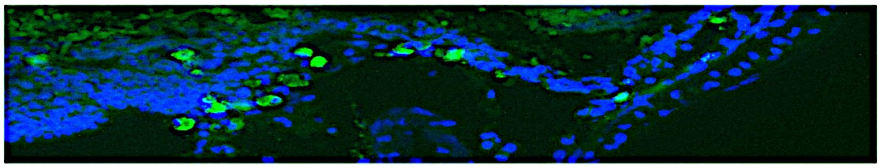

Anti-GFP IF

Choroid

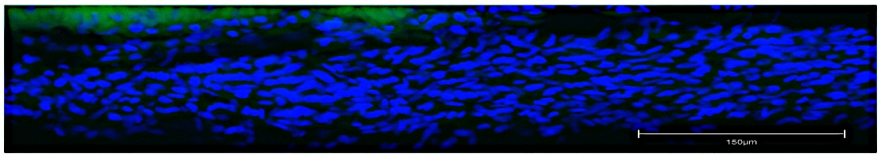

Secondary-only Control

FIGURE S4

Single-cell RNA seq Replicates

Tissue	Genotype	Replicate 1 (pooled tissue, tumors)	Replicate 2 (pooled tissue, tumors)
Skin	Wild-type	1 skin sample 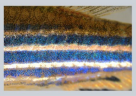	1 skin sample 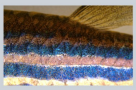
Skin Tumor	Wild-type	1 tumor sample 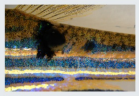 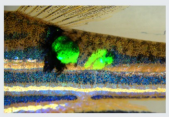	1 tumor sample 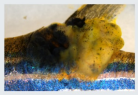 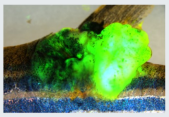
Eye Paired (tumor matched bilateral eye)	Wild-type	2 pooled eyes 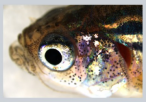 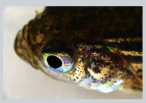	
Eye sibling matched	Wild-type	4 pooled eyes 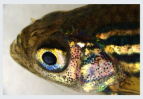 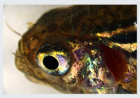 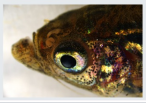	
Eye mock injected, sibling matched	Wild-type	3 pooled eyes 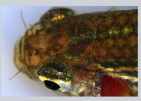 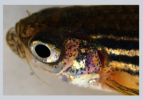 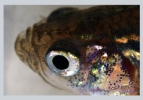	
Eye Tumor	Wild-type	1 tumor sample 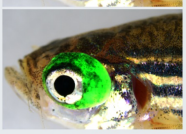	2 pooled tumor samples 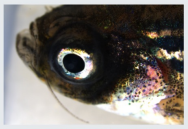 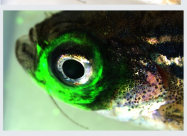 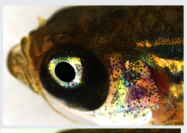 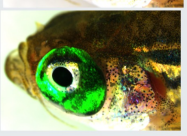

FIGURE S5

A

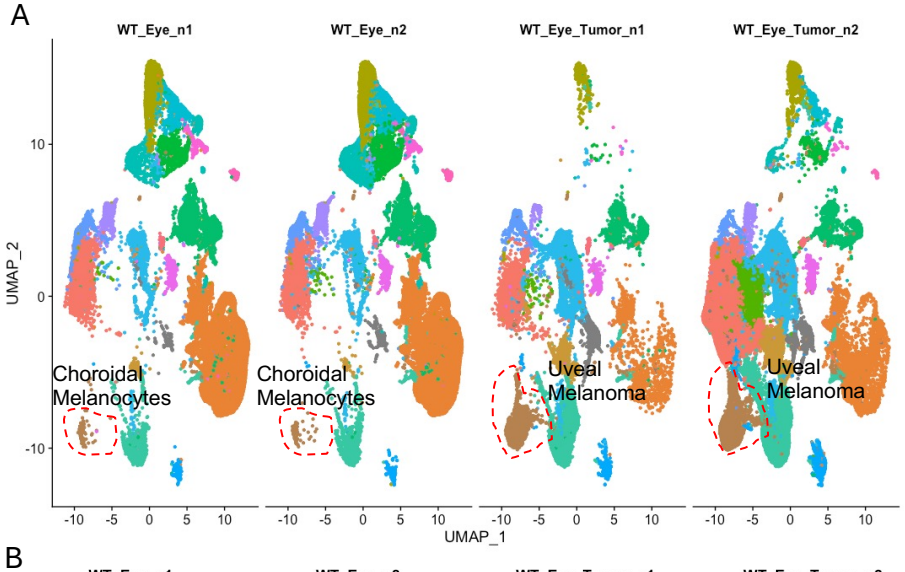
WT_Eye_n1
WT_Eye_n2
WT_Eye_Tumor_n1
WT_Eye_Tumor_n2
UMAP_2
UMAP_1
Choroidal Melanocytes
Choroidal Melanocytes
Uveal Melanoma
Uveal Melanoma

B

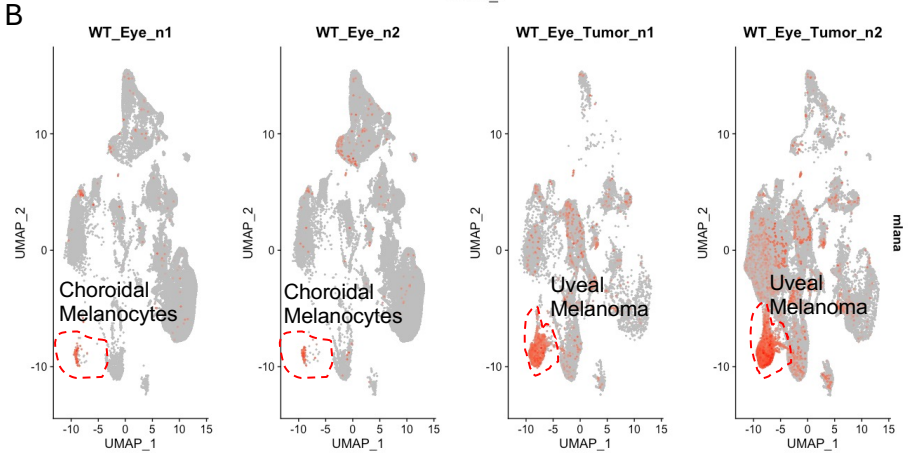
WT_Eye_n1
WT_Eye_n2
WT_Eye_Tumor_n1
WT_Eye_Tumor_n2
UMAP_2
UMAP_1
Choroidal Melanocytes
Choroidal Melanocytes
Uveal Melanoma
Uveal Melanoma
mlana

FIGURE S6

A

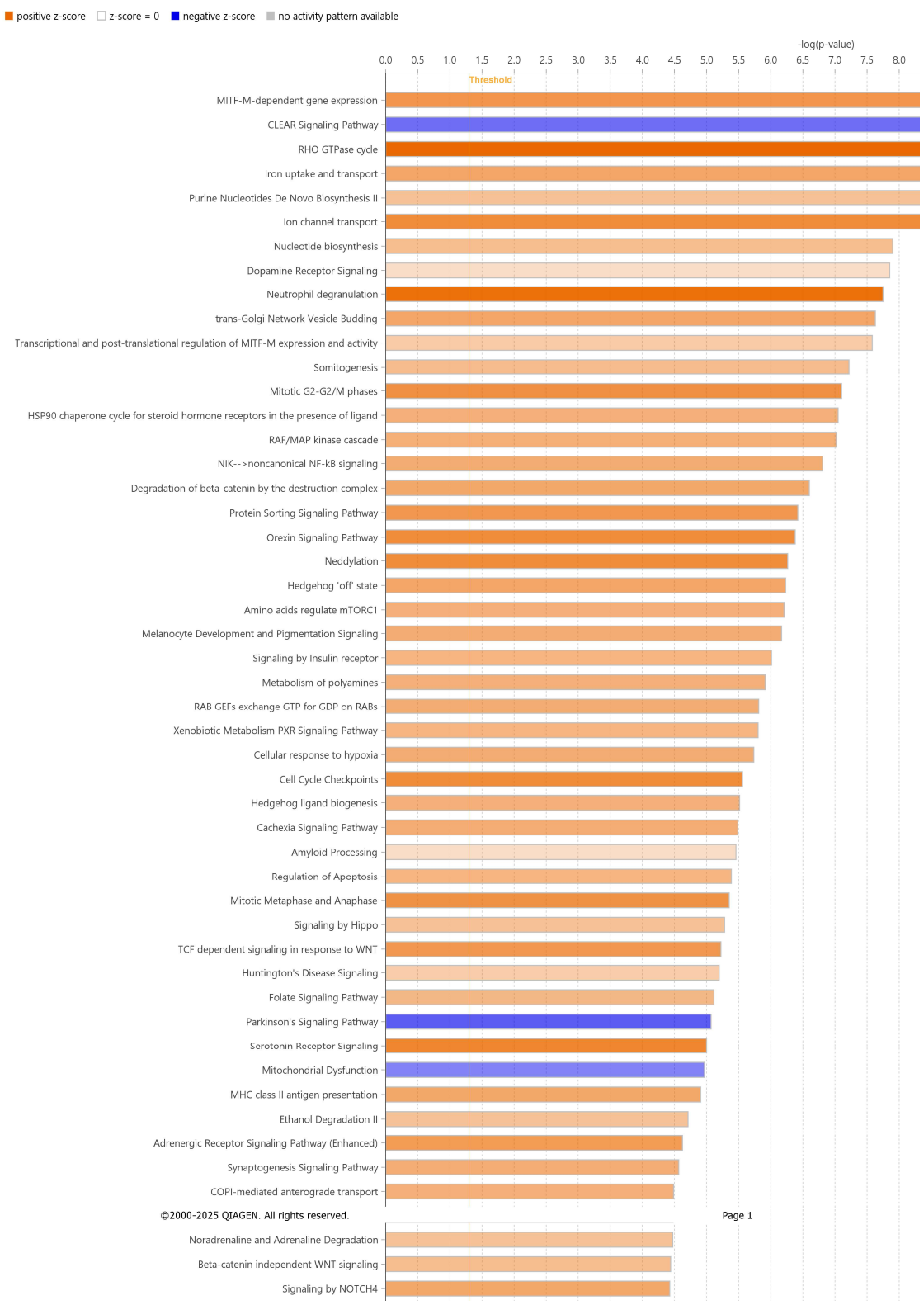
positive z-score
z-score = 0
negative z-score
no activity pattern available
-log(p-value)
0.0 0.5 1.0 1.5 2.0 2.5 3.0 3.5 4.0 4.5 5.0 5.5 6.0 6.5 7.0 7.5 8.0
Threshold
MITF-M-dependent gene expression
CLEAR Signaling Pathway
RHO GTPase cycle
Iron uptake and transport
Purine Nucleotides De Novo Biosynthesis II
Ion channel transport
Nucleotide biosynthesis
Dopamine Receptor Signaling
Neutrophil degranulation
trans-Golgi Network Vesicle Budding
Transcriptional and post-translational regulation of MITF-M expression and activity
Somitogenesis
Mitotic G2-G2/M phases
HSP90 chaperone cycle for steroid hormone receptors in the presence of ligand
RAF/MAP kinase cascade
NIK-->noncanonical NF-kB signaling
Degradation of beta-catenin by the destruction complex
Protein Sorting Signaling Pathway
Orexin Signaling Pathway
Neddylation
Hedgehog 'off' state
Amino acids regulate mTORC1
Melanocyte Development and Pigmentation Signaling
Signaling by Insulin receptor
Metabolism of polyamines
RAB GEFs exchange GTP for GDP on RABs
Xenobiotic Metabolism PXR Signaling Pathway
Cellular response to hypoxia
Cell Cycle Checkpoints
Hedgehog ligand biogenesis
Cachexia Signaling Pathway
Amyloid Processing
Regulation of Apoptosis
Mitotic Metaphase and Anaphase
Signaling by Hippo
TCF dependent signaling in response to WNT
Huntington's Disease Signaling
Folate Signaling Pathway
Parkinson's Signaling Pathway
Serotonin Receptor Signaling
Mitochondrial Dysfunction
MHC class II antigen presentation
Ethanol Degradation II
Adrenergic Receptor Signaling Pathway (Enhanced)
Synaptogenesis Signaling Pathway
COPI-mediated anterograde transport
©2000-2025 QIAGEN. All rights reserved.
Page 1
Noradrenaline and Adrenaline Degradation
Beta-catenin independent WNT signaling
Signaling by NOTCH4

B

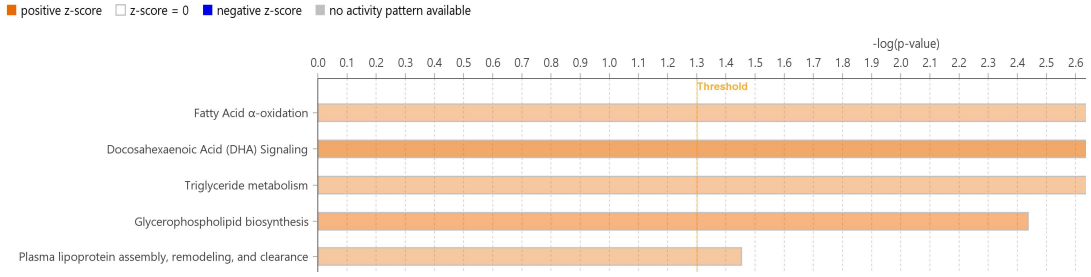
positive z-score
z-score = 0
negative z-score
no activity pattern available
-log(p-value)
0.0 0.1 0.2 0.3 0.4 0.5 0.6 0.7 0.8 0.9 1.0 1.1 1.2 1.3 1.4 1.5 1.6 1.7 1.8 1.9 2.0 2.1 2.2 2.3 2.4 2.5 2.6
Threshold
Fatty Acid α-oxidation
Docosahexaenoic Acid (DHA) Signaling
Triglyceride metabolism
Glycerophospholipid biosynthesis
Plasma lipoprotein assembly, remodeling, and clearance

FIGURE S7

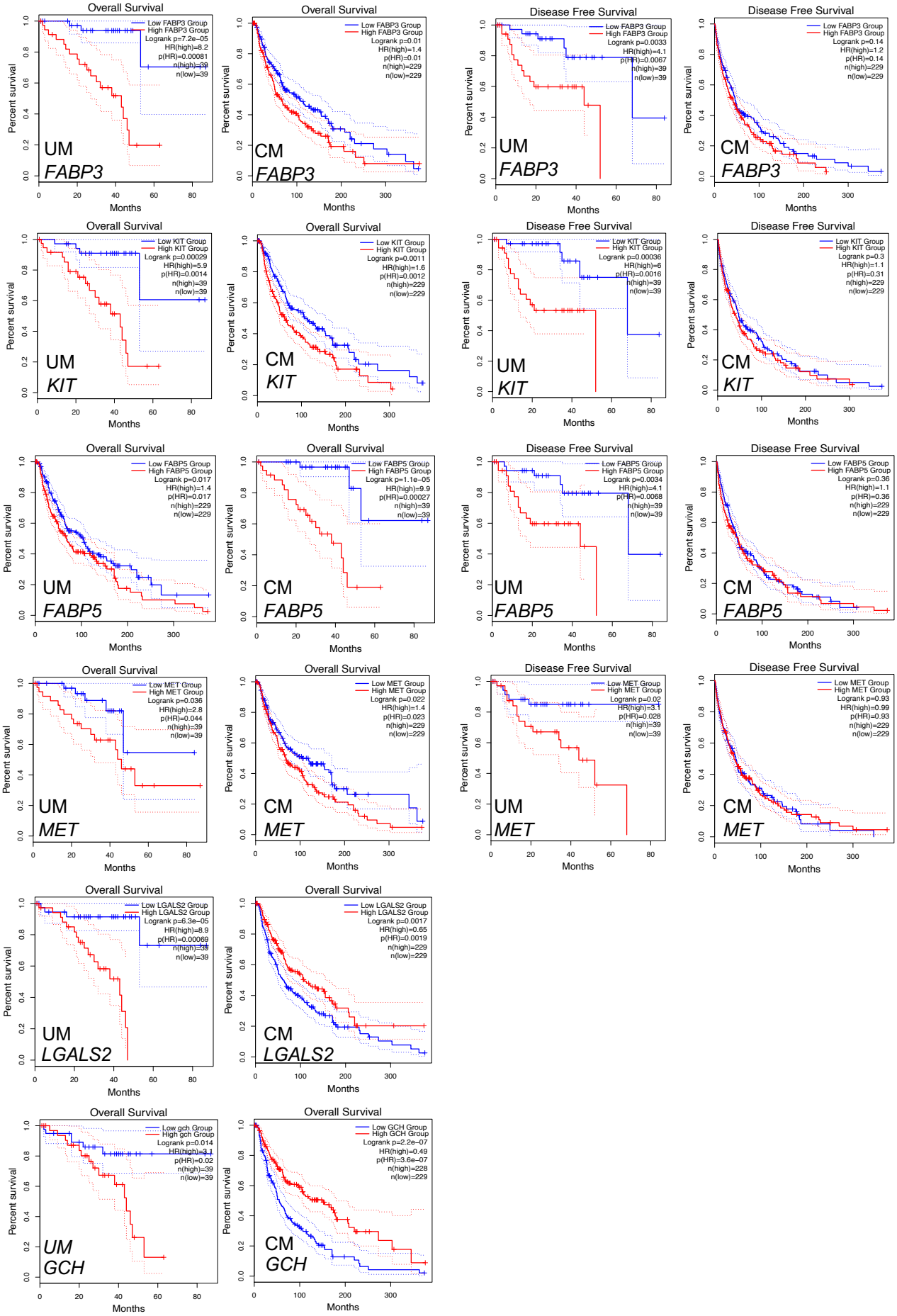
Overall Survival
Low FABP3 Group
High FABP3 Group
Logrank p=7.2e−05
HR(high)=8.2
p(HR)=0.00081
n(high)=39
n(low)=39
UM
FABP3
Overall Survival
Low FABP3 Group
High FABP3 Group
Logrank p=0.01
HR(high)=1.4
p(HR)=0.01
n(high)=229
n(low)=229
CM
FABP3
Disease Free Survival
Low FABP3 Group
High FABP3 Group
Logrank p=0.0033
HR(high)=4.1
p(HR)=0.0067
n(high)=39
n(low)=39
UM
FABP3
Disease Free Survival
Low FABP3 Group
High FABP3 Group
Logrank p=0.14
HR(high)=1.2
p(HR)=0.14
n(high)=229
n(low)=229
CM
FABP3
Overall Survival
Low KIT Group
High KIT Group
Logrank p=0.00029
HR(high)=5.9
p(HR)=0.0014
n(high)=39
n(low)=39
UM
KIT
Overall Survival
Low KIT Group
High KIT Group
Logrank p=0.0011
HR(high)=1.6
p(HR)=0.0012
n(high)=229
n(low)=229
CM
KIT
Disease Free Survival
Low KIT Group
High KIT Group
Logrank p=0.00036
HR(high)=6
p(HR)=0.0016
n(high)=39
n(low)=39
UM
KIT
Disease Free Survival
Low KIT Group
High KIT Group
Logrank p=0.3
HR(high)=1.1
p(HR)=0.31
n(high)=229
n(low)=229
CM
KIT
Overall Survival
Low FABP5 Group
High FABP5 Group
Logrank p=0.017
HR(high)=1.4
p(HR)=0.017
n(high)=229
n(low)=229
UM
FABP5
Overall Survival
Low FABP5 Group
High FABP5 Group
Logrank p=1.1e−05
HR(high)=9.9
p(HR)=0.00027
n(high)=39
n(low)=39
CM
FABP5
Disease Free Survival
Low FABP5 Group
High FABP5 Group
Logrank p=0.0034
HR(high)=4.1
p(HR)=0.0068
n(high)=39
n(low)=39
UM
FABP5
Disease Free Survival
Low FABP5 Group
High FABP5 Group
Logrank p=0.36
HR(high)=1.1
p(HR)=0.36
n(high)=229
n(low)=229
CM
FABP5
Overall Survival
Low MET Group
High MET Group
Logrank p=0.036
HR(high)=2.8
p(HR)=0.044
n(high)=39
n(low)=39
UM
MET
Overall Survival
Low MET Group
High MET Group
Logrank p=0.022
HR(high)=1.4
p(HR)=0.023
n(high)=229
n(low)=229
CM
MET
Disease Free Survival
Low MET Group
High MET Group
Logrank p=0.02
HR(high)=3.1
p(HR)=0.028
n(high)=39
n(low)=39
UM
MET
Disease Free Survival
Low MET Group
High MET Group
Logrank p=0.93
HR(high)=0.99
p(HR)=0.93
n(high)=229
n(low)=229
CM
MET
Overall Survival
Low LGALS2 Group
High LGALS2 Group
Logrank p=6.3e−05
HR(high)=8.9
p(HR)=0.00069
n(high)=39
n(low)=39
UM
LGALS2
Overall Survival
Low LGALS2 Group
High LGALS2 Group
Logrank p=0.0017
HR(high)=0.65
p(HR)=0.0019
n(high)=229
n(low)=229
CM
LGALS2
Overall Survival
Low gch Group
High gch Group
Logrank p=0.014
HR(high)=3.1
p(HR)=0.02
n(high)=39
n(low)=39
UM
GCH
Overall Survival
Low GCH Group
High GCH Group
Logrank p=2.2e−07
HR(high)=0.49
p(HR)=3.6e−07
n(high)=228
n(low)=229
CM
GCH
Percent survival
Months

FIGURE S8

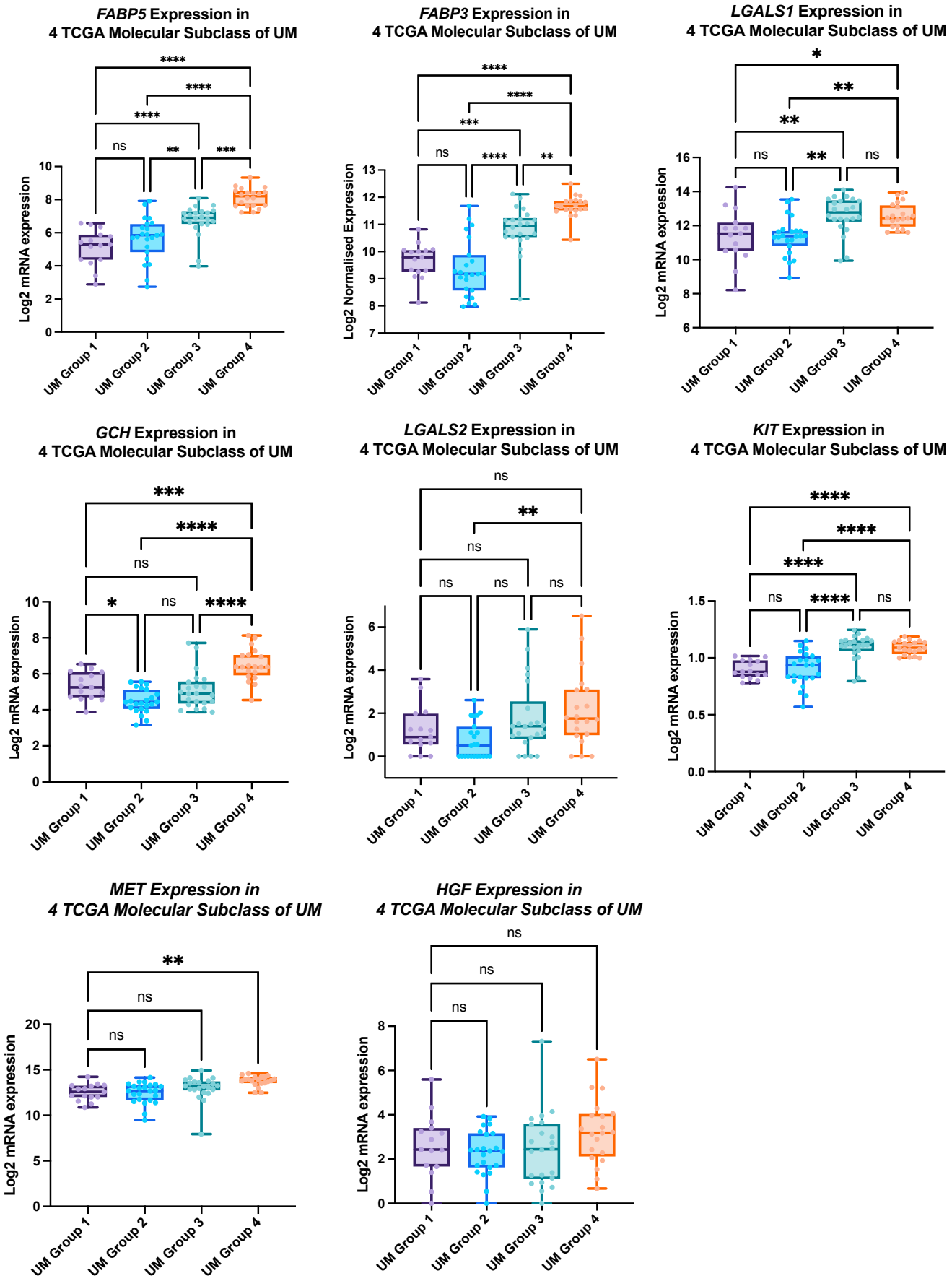
FABP5 Expression in 4 TCGA Molecular Subclass of UM
Log2 mRNA expression
FABP3 Expression in 4 TCGA Molecular Subclass of UM
Log2 Normalised Expression
LGALS1 Expression in 4 TCGA Molecular Subclass of UM
Log2 mRNA expression
GCH Expression in 4 TCGA Molecular Subclass of UM
Log2 mRNA expression
LGALS2 Expression in 4 TCGA Molecular Subclass of UM
Log2 mRNA expression
KIT Expression in 4 TCGA Molecular Subclass of UM
Log2 mRNA expression
MET Expression in 4 TCGA Molecular Subclass of UM
Log2 mRNA expression
HGF Expression in 4 TCGA Molecular Subclass of UM
Log2 mRNA expression
UM Group 1
UM Group 2
UM Group 3
UM Group 4
ns
*
**
***
****

FIGURE S9

A

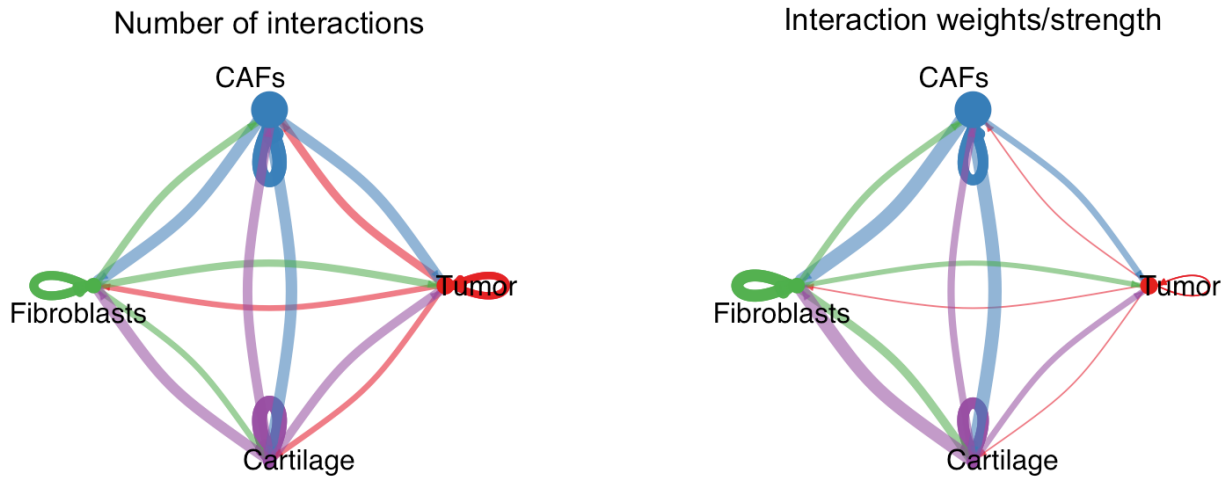

B

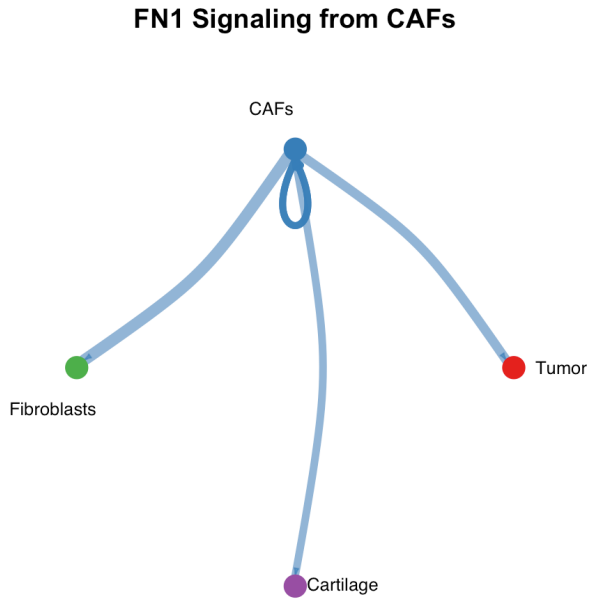

C

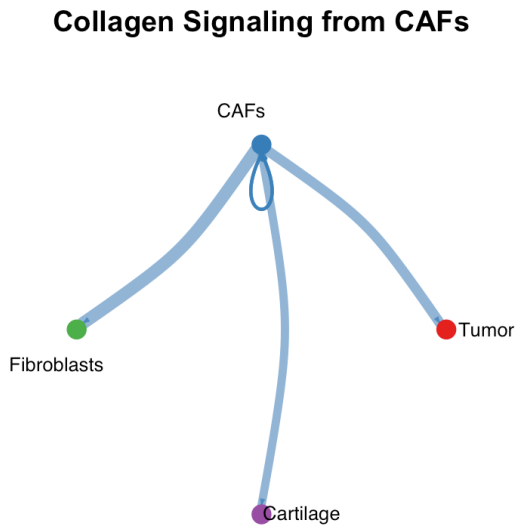

D

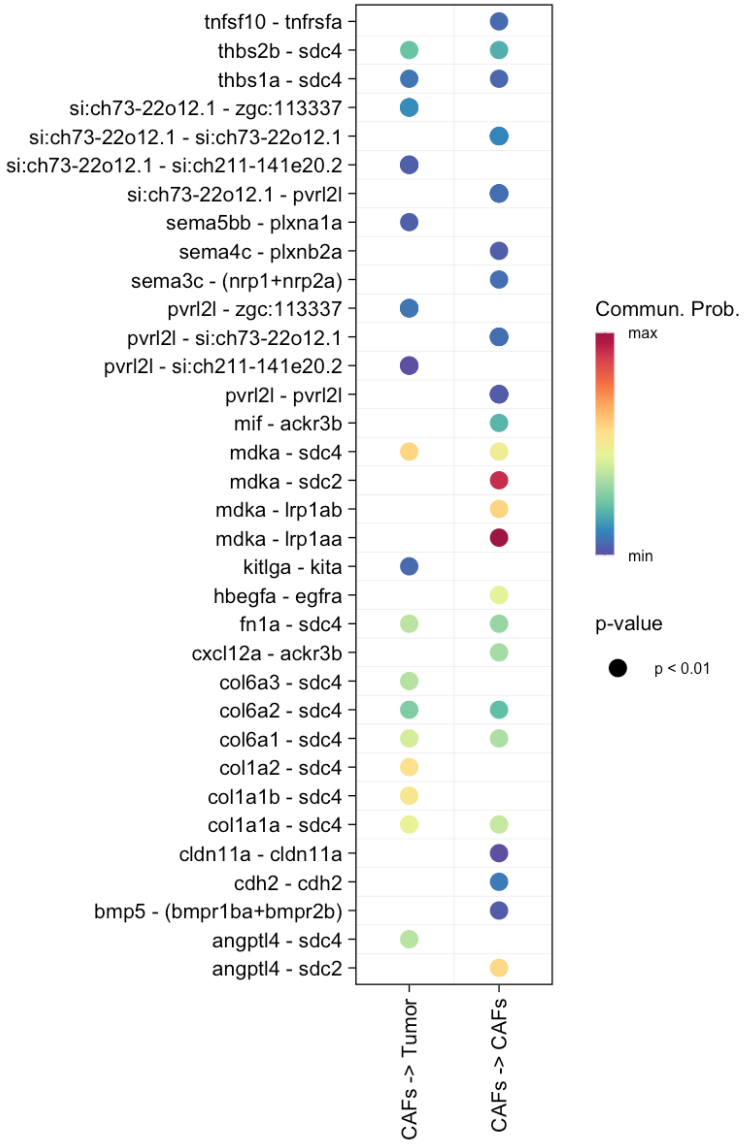

A

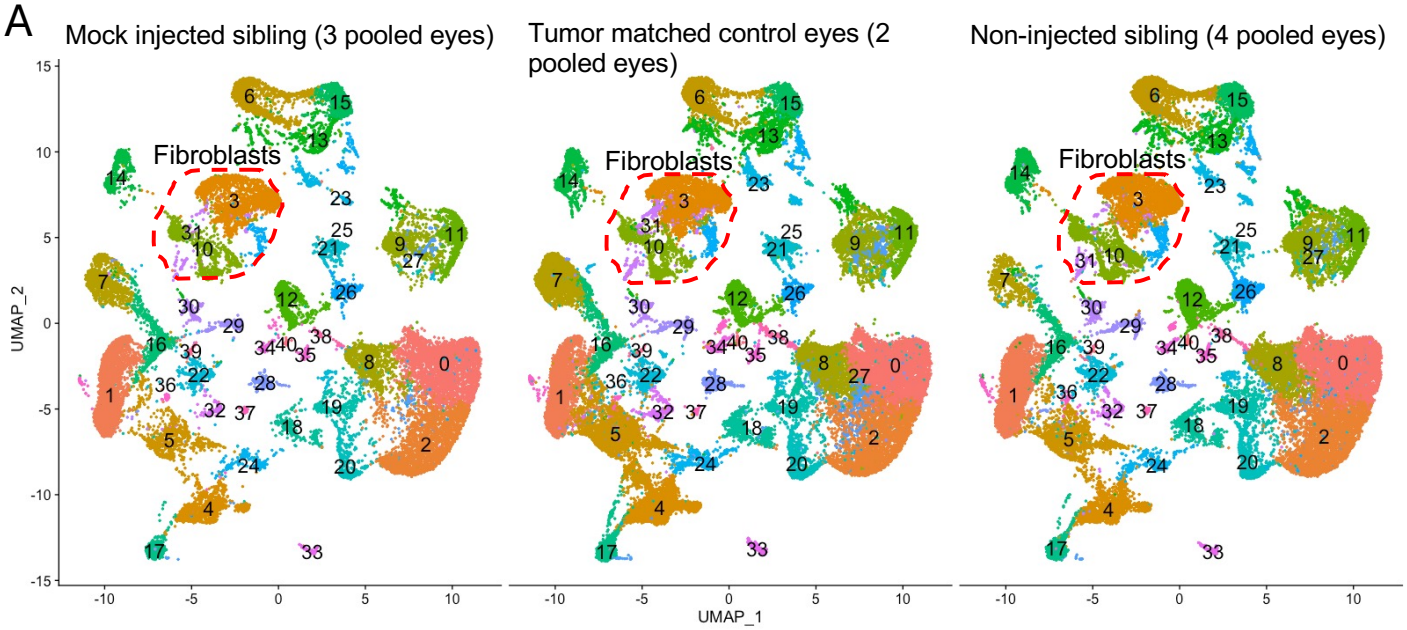
Mock injected sibling (3 pooled eyes)
Tumor matched control eyes (2 pooled eyes)
Non-injected sibling (4 pooled eyes)
Fibroblasts
UMAP_2
UMAP_1

B

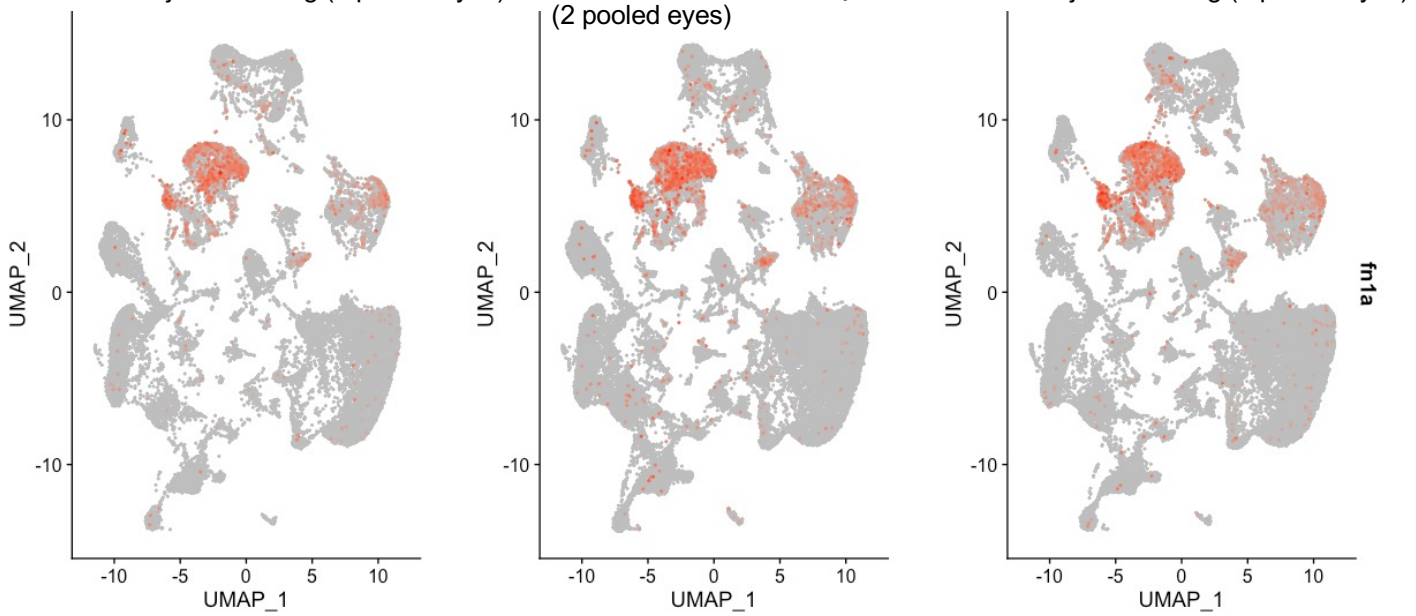
Mock injected sibling (3 pooled eyes)
Tumor matched control eyes (2 pooled eyes)
Non-injected sibling (4 pooled eyes)
fn1a
UMAP_2
UMAP_1

C

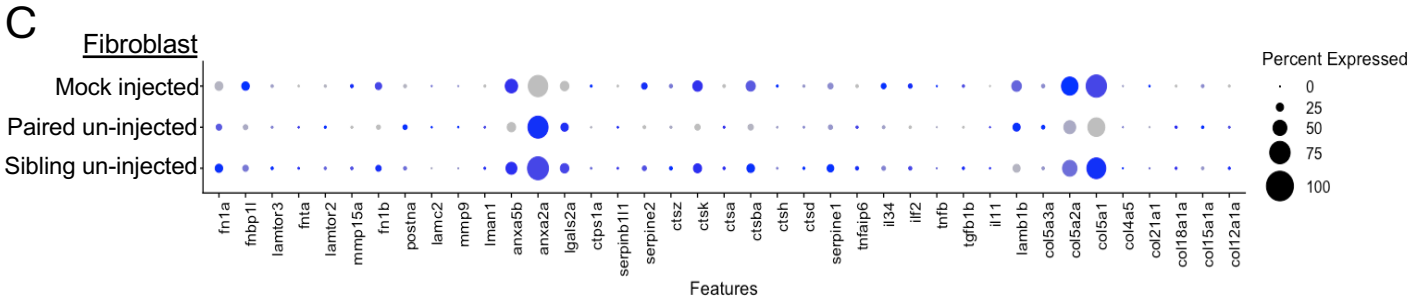
Fibroblast
Mock injected
Paired un-injected
Sibling un-injected
Percent Expressed
0
25
50
75
100
fn1a
fnbp1l
lamtor3
fnta
lamtor2
mmp15a
fn1b
postna
lamc2
mmp9
lman1
anxa5b
anxa2a
lgals2a
ctps1a
serpinb1l1
serpine2
ctsz
ctsk
ctsa
ctsba
ctsh
ctsd
serpine1
tnfaip6
il34
il2
tnfb
tgfb1b
il11
lamb1b
col5a3a
col5a2a
col5a1
col4a5
col21a1
col18a1a
col15a1a
col12a1a
Features

FIGURE S11

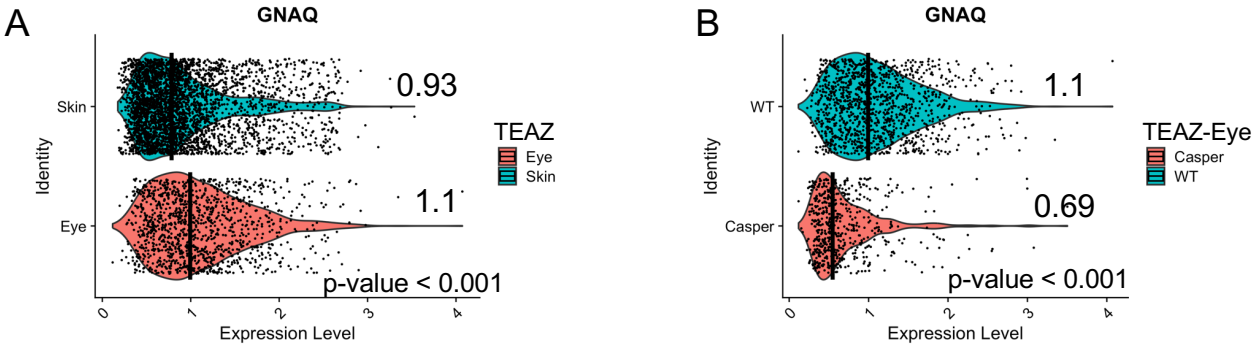
A
GNAQ
Skin
Eye
Identity
0.93
1.1
p-value < 0.001
0
1
2
3
4
Expression Level
TEAZ
Eye
Skin
B
GNAQ
WT
Casper
Identity
1.1
0.69
p-value < 0.001
0
1
2
3
4
Expression Level
TEAZ-Eye
Casper
WT

FIGURE S12

A

B

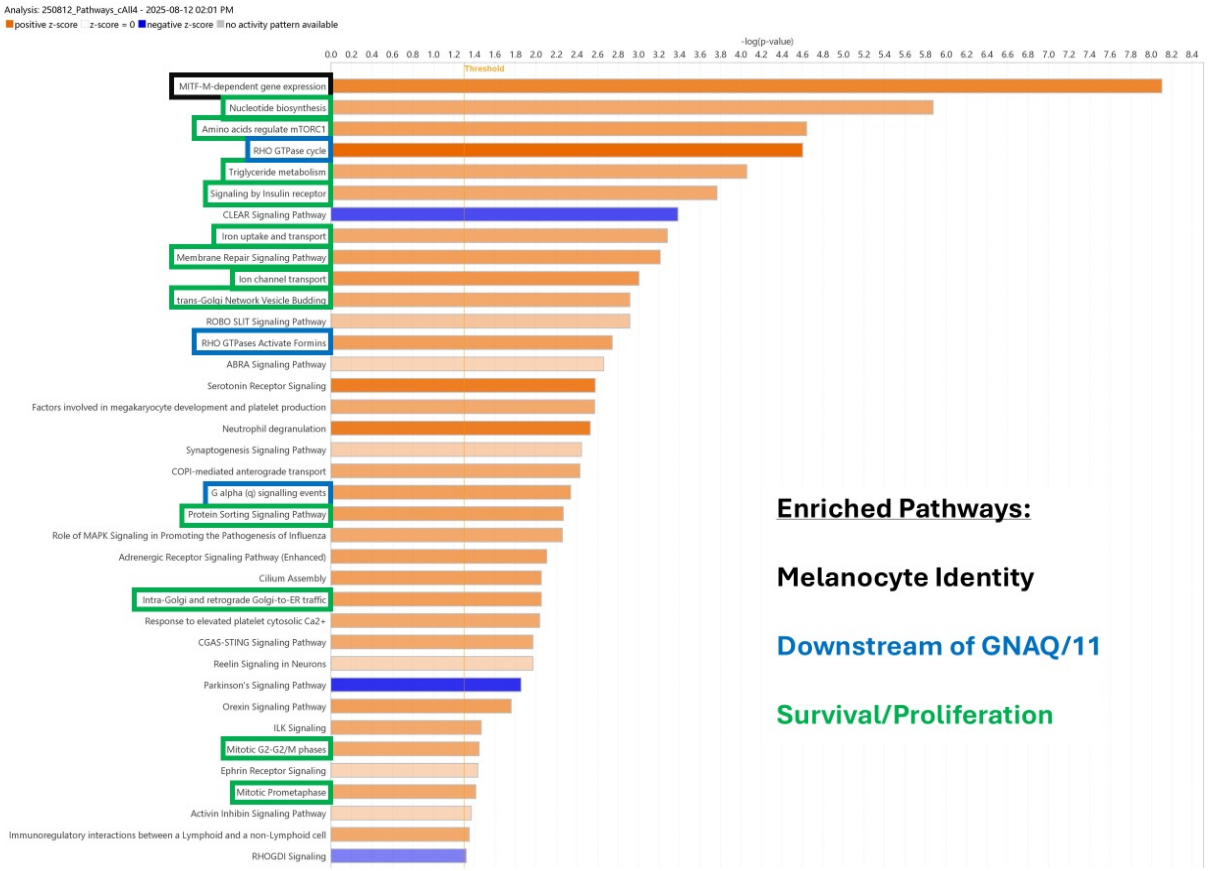

FIGURE S13

A Control injected: Wild type

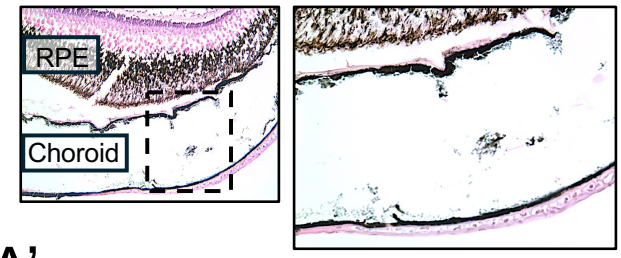

B Control injected: *nacre*

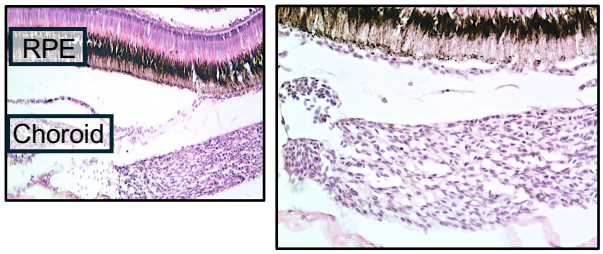

A' TEAZ-Eye (miniCoopR) : Wild type

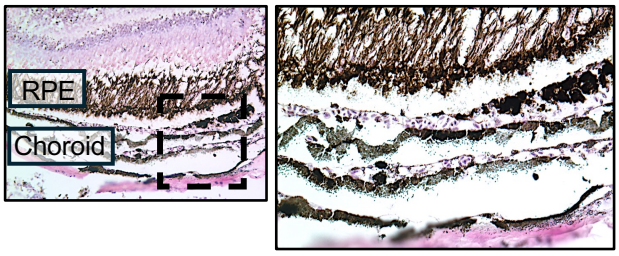

B' TEAZ-Eye (miniCoopR): *nacre*

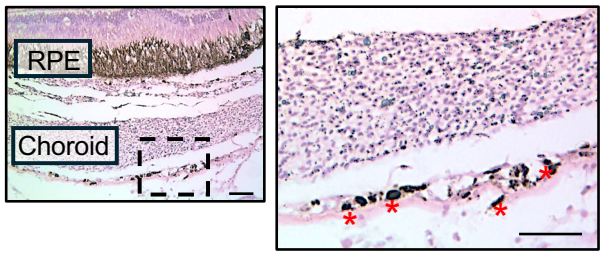

C TEAZ-Eye: (*mitfa:GNAQ*^{Q209L})

Tg(mitfa:GFP): mitfa$^{w2/w2}$

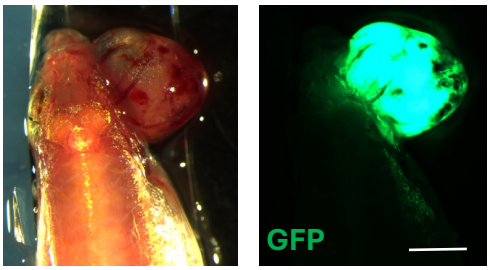

FIGURE S14
Single-cell RNA seq Replicates

Tissue	Genotype	Replicate 1 (pooled tissue, tumors)
Eye	Casper	3 pooled eyes
Eye Tumor	Casper	3 pooled tumors 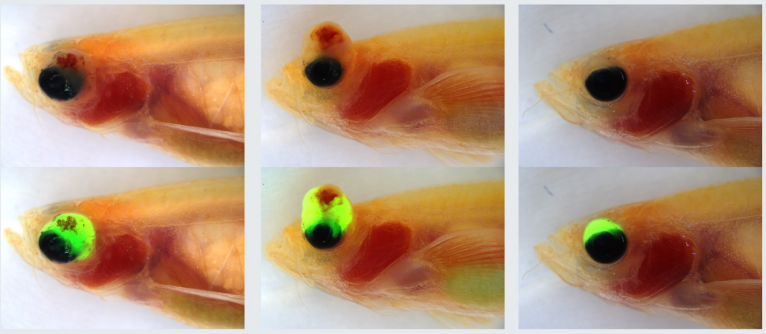
Whole embryo 28hpf	Wild-type Tg(mitfa-GFP); mitfa$^{+/w2}$	Pooled embryos 25 total 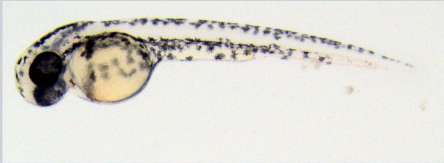
Whole embryo 28hpf	Nacre Tg(mitfa-GFP); mitfa$^{w2/w2}$	Pooled embryos 25 total 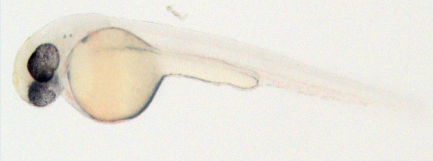

FIGURE S15

A

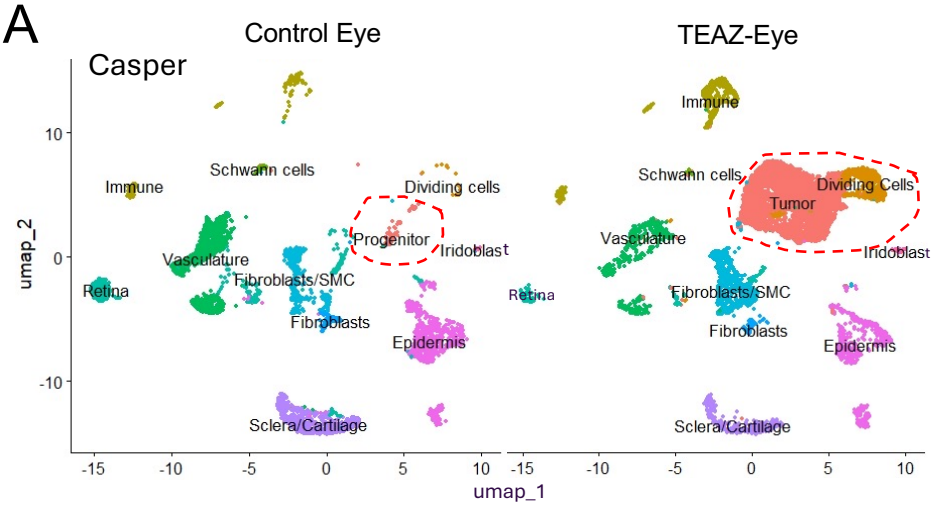

B

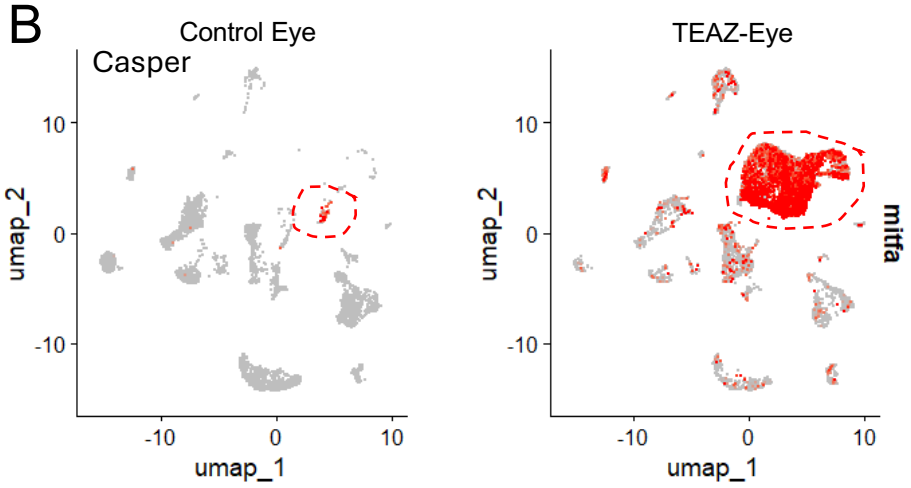

C

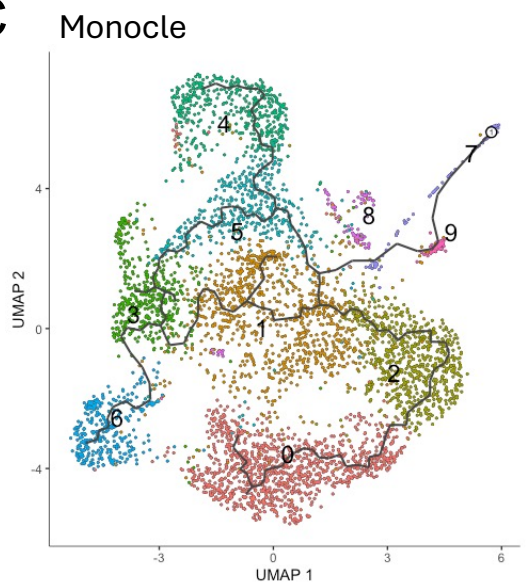

FIGURE S16

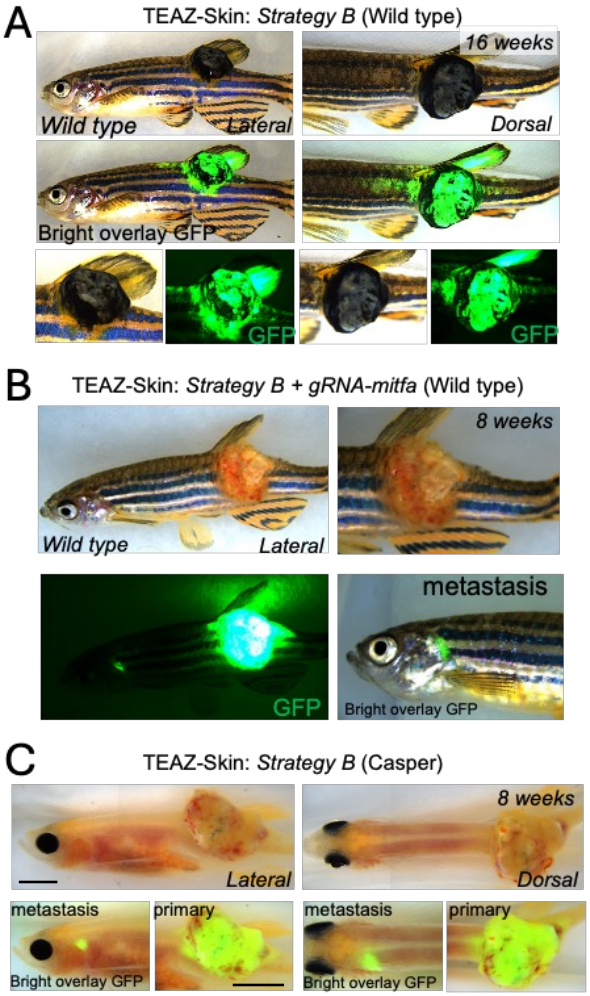
A
TEAZ-Skin: *Strategy B* (Wild type)
Wild type
Lateral
16 weeks
Dorsal
Bright overlay GFP
GFP
GFP
B
TEAZ-Skin: *Strategy B* + *gRNA-mitfa* (Wild type)
Wild type
Lateral
8 weeks
GFP
metastasis
Bright overlay GFP
C
TEAZ-Skin: *Strategy B* (Casper)
Lateral
8 weeks
Dorsal
metastasis
Bright overlay GFP
primary
metastasis
Bright overlay GFP
primary

FIGURE S17

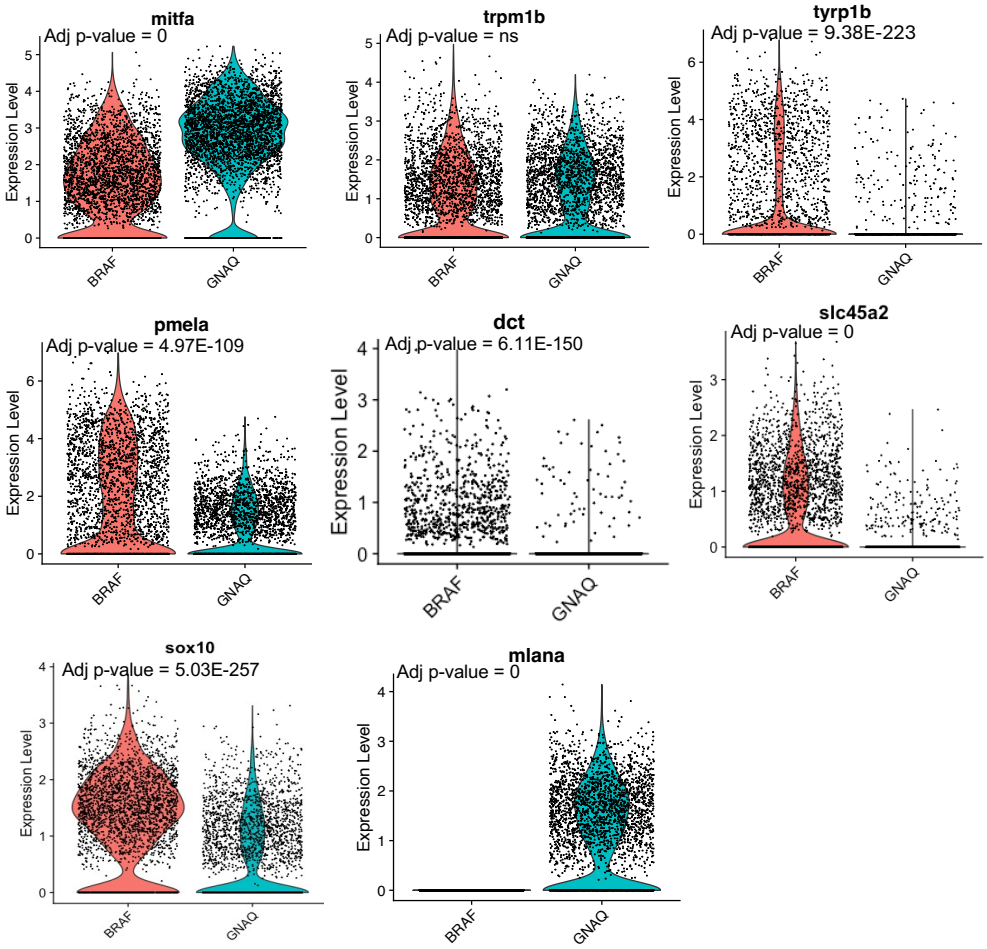
mitfa
Adj p-value = 0
trpm1b
Adj p-value = ns
tyrp1b
Adj p-value = 9.38E-223
pmela
Adj p-value = 4.97E-109
dct
Adj p-value = 6.11E-150
slc45a2
Adj p-value = 0
sox10
Adj p-value = 5.03E-257
mlana
Adj p-value = 0
Expression Level
BRAF
GNAQ

FIGURE S18

TEAZ-Eye Strategy B (Wild-type)

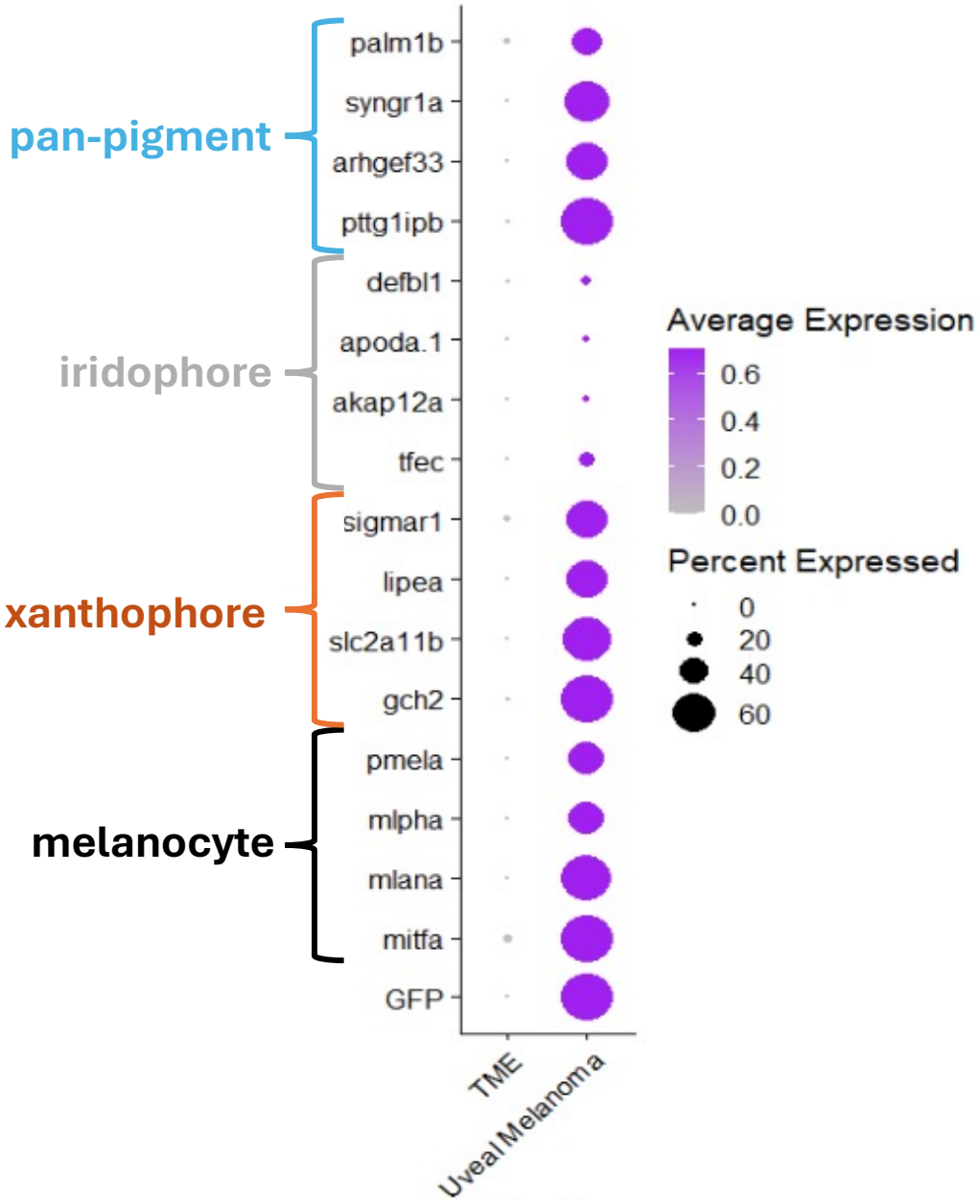

FIGURE S19

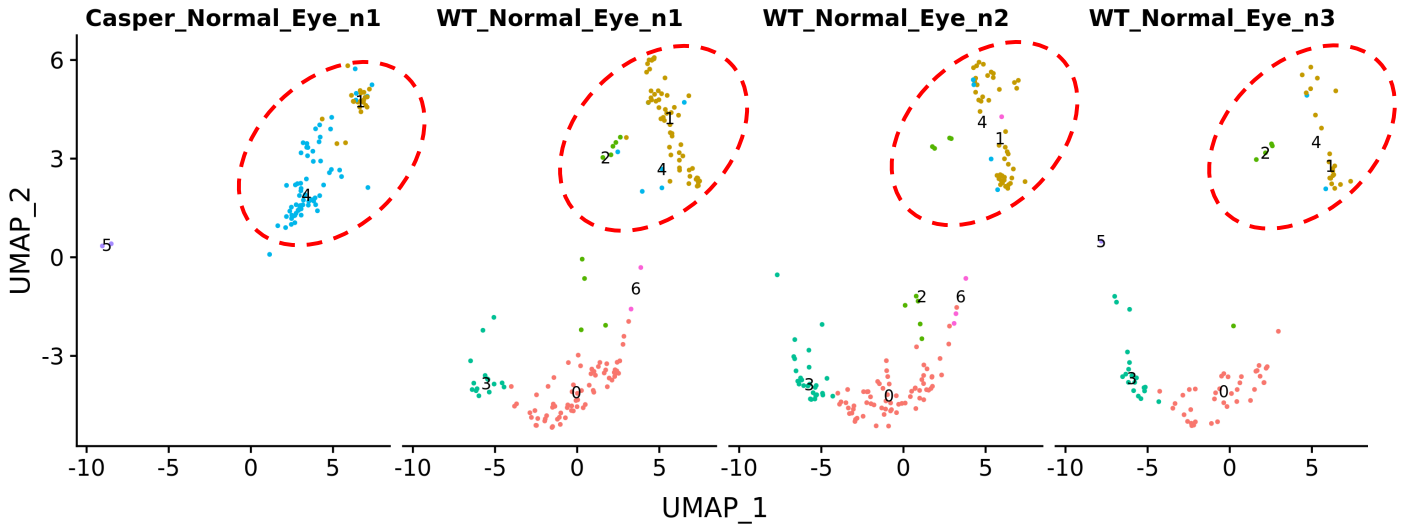
Casper_Normal_Eye_n1
WT_Normal_Eye_n1
WT_Normal_Eye_n2
WT_Normal_Eye_n3
UMAP_2
UMAP_1
6
3
0
-3
-10
-5
0
5

A

Mouse (Eye)

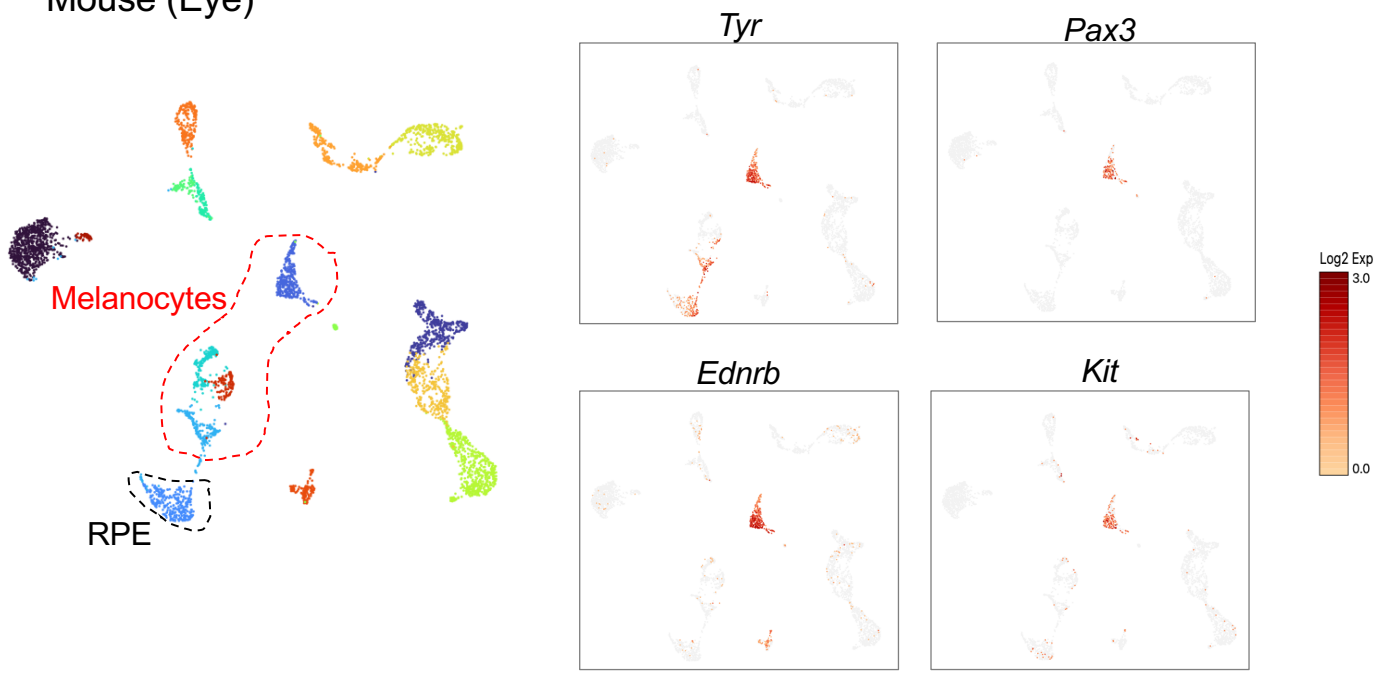

B

Human (Eye)

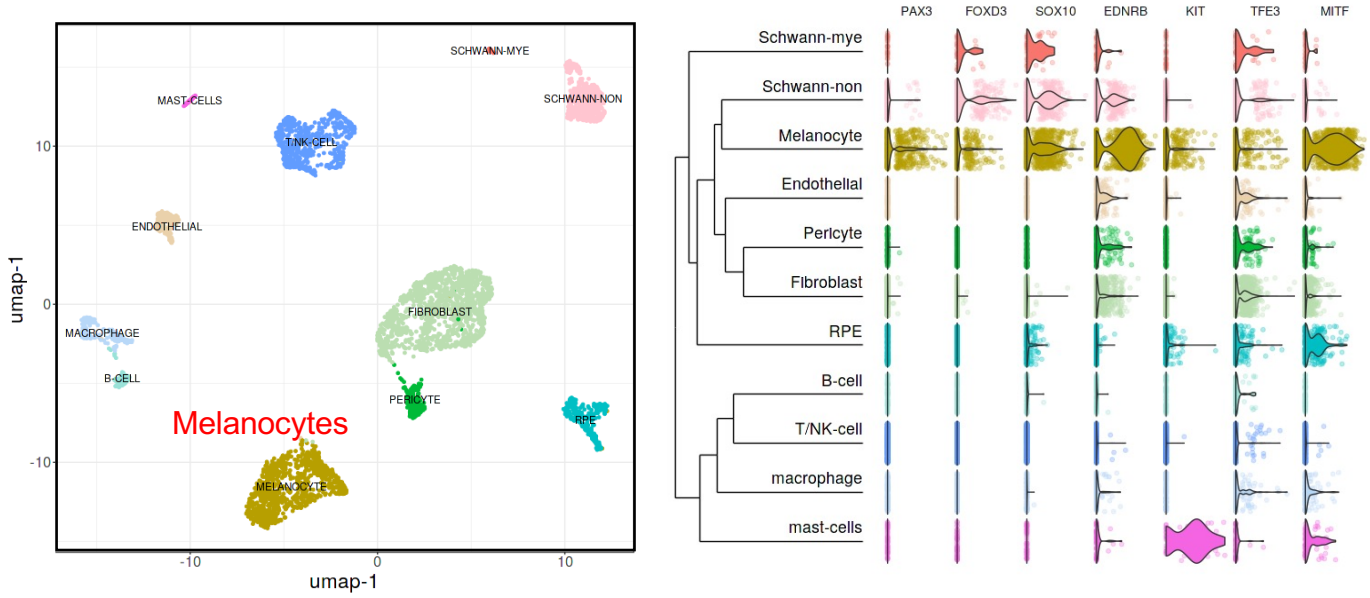
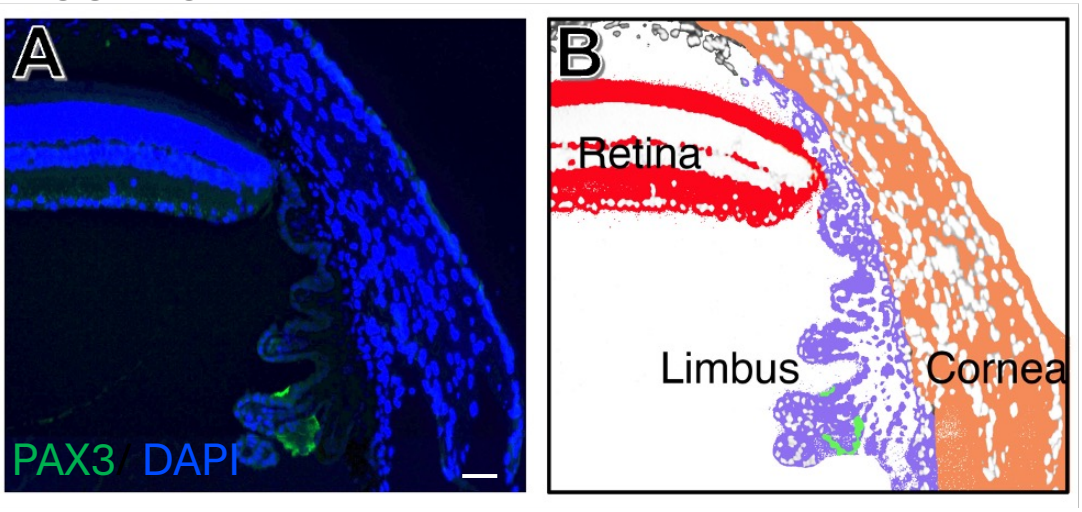
FIGURE S21